

Western diet increases COVID-19 disease severity in the Syrian hamster

Julia R. Port^{1*}, Danielle R. Adney^{1*}, Benjamin Schwarz², Jonathan E. Schulz¹, Daniel E.

Sturdevant³, Brian J. Smith⁴, Victoria A. Avanzato¹, Myndi G. Holbrook¹, Jyothi N.

Purushotham¹, Kaitlin A. Stromberg², Ian Leighton², Catharine M. Bosio², Carl Shaia⁴, Vincent J.

Munster^{1#}

1. Laboratory of Virology, National Institute of Allergy and Infectious Diseases, National Institutes of Health, Hamilton, MT, USA

2. Laboratory of Bacteriology, National Institute of Allergy and Infectious Diseases, National Institutes of Health, Hamilton, MT, USA

3. Genomics Unit, Research Technologies Branch, National Institute of Allergy and Infectious Diseases, National Institutes of Health, Hamilton, MT, USA

4. Rocky Mountain Veterinary Branch, Division of Intramural Research, National Institutes of Health, Hamilton, MT, USA

*These authors contributed equally

#Corresponding author: Vincent Munster, email: vincent.munster@nih.gov

24 **Summary (150 words)**

25 Pre-existing comorbidities such as obesity or metabolic diseases can adversely affect the clinical
26 outcome of COVID-19. Chronic metabolic disorders are globally on the rise and often
27 a consequence of an unhealthy diet, referred to as a Western Diet. For the first time in the Syrian
28 hamster model, we demonstrate the detrimental impact of a continuous high-fat high-sugar diet
29 on COVID-19 outcome. We observed increased weight loss and lung pathology, such as exudate,
30 vasculitis, hemorrhage, fibrin, and edema, delayed viral clearance and functional lung recovery,
31 and prolonged viral shedding. This was accompanied by an increased trend of systemic IL-10
32 and IL-6, as well as a dysregulated serum lipid response dominated by polyunsaturated fatty acid-
33 containing phosphatidylethanolamine, recapitulating cytokine and lipid responses associated with
34 severe human COVID-19. Our data support the hamster model for testing restrictive or targeted
35 diets and immunomodulatory therapies to mediate the adverse effects of metabolic disease on
36 COVID-19.

37

38 **Keywords:** Syrian hamster, SARS-CoV-2, obesity, pathogenesis, lipid metabolism

39 **Introduction**

40 Severe acute respiratory syndrome coronavirus-2 (SARS-CoV-2) is the etiological agent of
41 coronavirus disease (COVID)-19 and can cause asymptomatic to severe lower respiratory tract
42 infections in humans (Nie et al., 2020; Parry et al., 2020). Pre-existing comorbidities such as
43 immunosuppression, obesity, diabetes, or chronic lung disease can adversely affect the clinical
44 outcome (Butler and Barrientos, 2020; Hussain et al., 2020; Li et al., 2009; Petrakis et al., 2020).
45 Of these, obesity and metabolic disorders are global pandemics of rising concern (Araújo et al.,
46 2019; Saklayen, 2018; Swinburn et al., 2011). The underlying disease is driven mainly by changes
47 in the global food system, which is producing more processed, affordable, and effectively
48 marketed food than ever before. This diet, rich in saturated fats and refined sugars, is referred to
49 as a Western Diet (Cordain et al., 2005). Long-term consumption of a Western Diet may result in
50 chronic activation of the immune system, impairing both innate and adaptive responses (Green
51 and Beck, 2017a, b; Rogero and Calder, 2018). The Western Diet has been associated with non-
52 alcoholic steatohepatitis (NASH) and non-alcoholic fatty liver disease (NAFLD). These disease
53 syndromes predispose individuals to multiple comorbidities that can include cirrhosis and liver
54 failure. The relative risk of hospitalization and severe COVID-19 outcome are significantly
55 increased for patients afflicted by these comorbidities (Butler and Barrientos, 2020). This has
56 resulted in disproportionately worse outcomes in US ethnic and racial minorities, where
57 prevalence and incidence of metabolic disorders are increased (Cefalu and Rodgers, 2021).

58 It is currently unclear how certain comorbidities may determine disease manifestation of COVID-
59 19. Different studies have demonstrated that the Syrian hamster model is suitable to model
60 aspects of obesity and diabetes and for studying lipid metabolism (Dalbøge et al., 2015; Kasim-
61 Karakas et al., 1996). In healthy hamsters, SARS-CoV-2 infection is associated with mild to
62 moderate clinical disease (Chan et al., 2020; Rosenke et al., 2020; Sia et al., 2020). However, no
63 studies have investigated COVID-19 in hamsters with comorbidities. Here we show in a Syrian
64 hamster model how a continuous high-fat high-sugar (HFHS) diet changed the metabolomic state

65 in the Syrian hamster and the resulting consequences on viral replication dynamics, immune
66 protection and disease severity after infection with SARS-CoV-2.

67

68 **Results**

69 **High-fat and high-sugar diet induces metabolic changes characterized by increased early** 70 **weight gain and glucose tolerance**

71 We investigated the impact of a consistent high-fat and high-sugar (HFHS) diet on the Syrian
72 hamster. Either a regular rodent (RD) diet or a high-calorimetric HFHS diet was given to male
73 Syrian hamsters (4-6 week old) for 16 weeks *ad libitum* (N = 35, respectively). Weight gain of
74 juvenile hamsters was monitored weekly. Initially, animals on the HFHS diet gained weight faster
75 than animals on the regular diet. Difference in median weights was significant from the 2nd week
76 onwards until week 10 (**Fig 1 A**, N = 35, ordinary two-way ANOVA, followed by Sidak's multiple
77 comparisons test, p = 0.001, p = <0.001, p = <0.001, p = <0.001, p = <0.001, p = <0.001, p =
78 <0.001, p = 0.0011, p = <0.001). After week 10 weight gain either plateaued or decreased in the
79 HFHS group (median = 165 g), while in the regular diet group weight increased until week 12
80 (median = 160 g), at which point the median weight between groups showed no significant
81 difference. We observed morbidity (4/35 = 11%) in the HFHS group, which was absent in the RD
82 group.

83 To assess the levels of glucose-associated symptoms triggered by a HFHS diet we conducted an
84 oral glucose tolerance test (OGTT). No difference in fasting blood glucose levels between diet
85 groups was observed (N = 30 (RD) / 29 (HFHS), median = 150 / 147 mg/dL). However, HFHS
86 animals demonstrated impaired glucose intolerance upon application of an oral glucose dose;
87 blood glucose levels 30 min, 60 min and 120 min after oral application were significantly increased
88 compared to RD animals (**Fig 1 B**, N = 30 (RD) / 29 (HFHS), 30 minutes median = 265 / 313
89 mg/dL and 60 minutes median = 290 / 347 mg/dL, ordinary two-way ANOVA, followed by Sidak's
90 multiple comparisons test, p = 0.0004, p = 0.0009, respectively). We compared the insulin

91 response after application of oral glucose load and found no difference between the diet regimens.
92 The insulin resistance index (fasting glucose level (mmol/L) x fasting insulin level (mIU/L) showed
93 no significant differences (**Fig 1 C**, N = 30 (RD) / 29 (HFHS), Mann-Whitney test, $p = 0.6871$)
94 (Hayashi et al., 2013; Li et al., 2009). Five animals were euthanized pre-challenge in order to
95 assess diet induced pathology. There was no difference in body fat-to-weight ratio (**Fig 1 D**, N =
96 5, median = 1.905 (RD) / 2.117 (HFHS) Fat:Bodyweight ratio (mg/g), Mann-Whitney test, $p >$
97 0.9999).

98

99 **High-fat and high-sugar diet induces liver damage and systemic hyperlipidemia**

100 We investigated the changes in lipid metabolism through a blood lipid biochemistry panel (**Sup**
101 **Table 1**). Due to increased levels of fat in the samples collected from HFHS animals, HDL and
102 LDL could not be assessed due to incompatibility with the instrument. Total cholesterol was
103 significantly increased in the HFHS group (**Fig 1 E**, N = 10 (RD) / 7 (HFHS), median = 67.6 / 380
104 mg/dL, Mann-Whitney test, $p = 0.0001$). The median (146 U/L) alanine aminotransferase (ALT),
105 an indication of hepatocellular injury without overt cholestasis, values in the HFHS animals were
106 above the upper limit of previously established reference ranges (Washington and Van Hoosier,
107 2012). To understand which lipids were circulating in serum, we analyzed serum by liquid
108 chromatography tandem mass spectrometry (LC-MS/MS). Aggregate signals across all lipid
109 classes assayed in the HFHS animals compared to RD were increased, comprising
110 phospholipids, cholesterol esters, sphingolipids, neutral lipids, lysophospholipids, and free fatty
111 acids (**Fig 1 F**, N = 5(RD) / 4 (HFHS), Mann-Whitney test, $p = 0.0159$, $p = 0.0635$, $p = 0.0159$, p
112 $= 0.0317$, $p = 0.0653$, $p = 0.0317$, respectively). Hence, we further assessed changes in the liver
113 through gross and histologic pathology. Gross pathology of livers differed substantially. Livers
114 from animals on the HFHS diet were diffusely pale, friable, and sections floated in formalin while
115 RD hamster livers appeared grossly normal. Histologically, hepatocytes were expanded by micro

116 and macrovesicles in HFHS animals, while hepatocytes in RD animals appeared normal (**Fig 2 A**
117 **- F**).

118 To further characterize the effect of the HFHS diet regimen on the liver, we evaluated global
119 changes in the gene expression after 16 weeks. Principal components analysis of the complete
120 gene expression profile revealed expected grouping with each diet regimen group containing their
121 associated replicates (**Sup Fig 1 A**, N = 5 (RD), 4 HFHS). In total, 2,114 genes were significantly,
122 differentially expressed ($p < 0.05$ and > 2 fold) in the liver. To assess the enrichment of these
123 differential genes, they were imported into Ingenuity Pathway Analysis (IPA) software. The results
124 show that in the comparison of HFHS to RD animals 124 canonical pathways were significantly
125 enriched and 200 downstream effects were predicted on biological processes and disease or
126 toxicological function (p -value < 0.05 , z -score ≤ -2 or ≥ 2): amongst which were cell recruitment,
127 inflammation, activation, and immune-associated pathways (**Fig 2 G**, **Sup Table 2** shows all
128 significant predicted downstream effects). Interestingly, we also observed a pathway activation
129 pattern reminiscent of NAFLD TNF-driven inflammation, (**Fig 2 H**).

130 Together, these data suggest that HFHS diet induced drastic changes in glucose uptake and lipid
131 metabolism, characterized by systemic dyslipidemia and gross changes in liver pathology. This
132 translated into increased inflammation and a gene expression profile in the liver reminiscent of
133 fatty liver disease.

134

135 **High-fat and high-sugar diet exacerbated disease severity after SARS-CoV-2 infection**

136 We challenged hamsters (RD: N = 20, HFHS = 13 (Group size adjusted for the HFHS group due
137 to the morbidity of the model pre-challenge)) with 8×10^4 TCID₅₀ SARS-CoV-2 via the intranasal
138 route. Animals were euthanized at 7 days-post inoculation (DPI) (RD: N = 10, HFHS = 4), at 14
139 DPI (RD: N = 5, HFHS = 4) or monitored until 21 DPI (RD: N = 5, HFHS = 5). We observed a
140 trend of more severe morbidity in the HFHS group, in which two animals reached euthanasia
141 criteria ($> 20\%$ relative body weight loss) at 8 and 9 DPI, respectively (**Fig 3 A**). While the HFHS

142 animals demonstrated non-infection associated morbidity, the timing and symptoms associated
143 with these fatalities suggest that they were caused by the infection. In the RD group, a median
144 peak weight loss was observed at 6 DPI (~7% relative body weight), after which animals
145 recovered and returned to pre-challenge weights by 14 DPI. Weight in HFHS animals was
146 significantly decreased after 3 DPI and negative area under the curve (AUC) analysis between 1
147 -14 DPI revealed significant difference (**Fig 3 B**, N = 10 (RD) / 7 (HFHS), Mann-Whitney test, p =
148 0.0002). In the HFHS group median peak weight loss was reached at 8 DPI (~16% relative body
149 weight) and no animal recovered pre-challenge weights until the end of the study at 21 DPI.

150 To better understand the clinical impact of a HFHS diet on SARS-CoV-2 infection, the respiratory
151 function of the hamsters was evaluated. We performed forced oscillation tests on mechanically
152 ventilated hamsters pre-challenge, and on 7, 14, and 21 DPI. No significant differences in
153 pulmonary function were detected between the RD and HFHS groups at any time point.

154 Pulmonary function after SARS-CoV-2 infection has not been assessed in the Syrian hamster yet,
155 so we combined the groups to evaluate changes over the course of infection. Inspiratory capacity
156 was significantly decreased in 7 DPI as compared to pre-challenge (**Figure 3 C**, baseline: N = 5
157 (RD) / 3 (HFHS) and 7 DPI: N = 5 (RD) / 4 (HFHS), baseline median = 4.345 / 4.032 and 7 DPI
158 median = 3.195 / 3.464 mL, ordinary two-way ANOVA, followed by Tukey's multiple comparisons
159 test, p = 0.0107). Elastance of the respiratory system was significantly increased at 7 DPI
160 (baseline median = 2.68 / 3.032 and 7 DPI median = 4.138 / 3.852 cmH₂O/mL, p = 0.0022), as
161 was tissue elastance (baseline median = 2.514 / 2.450 and 7 DPI median = 3.021 / 3.217
162 cmH₂O/mL, p = 0.0040). The resistance of the airway not associated with gas exchange
163 (Newtonian resistance) was not significantly different at any time point; however total resistance
164 was significantly increased in 7 DPI as compared to pre-challenge (baseline median = 0.151 /
165 0.167 and 7 DPI median = 0.181 / 0.205 cmH₂O.s/mL, p = 0.034). Changes in peripheral
166 resistance were also detected by an increase in tissue damping at 7 DPI as compared to pre-
167 challenge animals, which reflects how oscillatory energy is dispersed or retained within

168 parenchymal tissue (baseline median = 0.564 / 0.623 and 7 DPI median = 0.695 / 0.720
169 cmH₂O/mL, $p = 0.0158$). Recovery to pre-challenge was observed for all parameters by 14 DPI.
170 Together, these changes in respiratory function led to an overall decrease in shape parameter k ,
171 which reflects the curvature of the pressure-volume curve, on 7 DPI (**Fig 3 D**, baseline median =
172 0.193 / 0.180 and 7 DPI median = 0.168 / 0.158 /cmH₂O, ordinary two-way ANOVA, followed by
173 Sidak's multiple comparisons test, $p = 0.0001$). While not significant, a slower trend of recovery
174 to pre-challenge values for resistance and tissue damping was observed in the HFHS group. This
175 could indicate that functional lung recovery in this group was slower.

176

177 **High-fat and high-sugar diet is associated with exudate, vasculitis, inflammation of the**
178 **epithelia and hemorrhage, fibrin and edema, and decreased viral clearance**

179 Next, we assessed the pathology in the lungs at necropsy, 7 DPI. Grossly, lungs displayed lesions
180 with multifocal dark red foci visible on the surface of the lobes (**Fig 4 A-J**). Across groups the 7
181 DPI lungs were more turgid, failed to collapse and had increased lung weights as compared to
182 pre-challenge lungs (**Sup Fig 2 A**). Lung weight recovery appeared slower in HFHS animals.
183 Histopathologically, only a subset of RD animals demonstrated increased lung damage ($N = 5/10$,
184 $> 50\%$ lung tissue affected). At 7 DPI, foci were multifocal and adjacent to bronchi and blood
185 vessels as well as peripherally along the sub pleural margin. Overall, no significant difference
186 was seen between the cumulative pathological score between diet groups. However, three out of
187 four animals demonstrated lesions in $>50\%$ of tissue (**Fig 4 K, Sup Fig 2 B**). In HFHS animals,
188 foci were multifocal but less clearly delineated due to hemorrhage, edema, and fibrin. Interstitial
189 pneumonia was characterized by thickened septa due to inflammatory cells, fibrin and edema and
190 lined by hyperplastic type II pneumocytes. Alveoli were filled with inflammatory cells, edema and
191 organizing fibrin. The two HFHS animals which were euthanized at day 8/9 due to severe disease
192 and weight loss ($>20\%$) both showed pneumonia, hemorrhage, edema, and inflammation (**Sup**
193 **Fig 3**).

194 At 14 DPI, thickened septa, presumably from interstitial fibrosis with alveolar bronchiolization,
195 were observed in lungs from RD animals (N = 2) (**Sup Fig 4 A-D**). In contrast, HFHS animals at
196 14 DPI had less septal thickening and more septal, alveolar, and perivascular inflammation (N =
197 2). At 21 DPI four out of five of the RD animals and three out of three of the HFHS animals had
198 thickened alveolar septa with alveolar bronchiolization (**Sup Fig 4 E-H**).

199 Immunohistochemistry staining for SARS-CoV-2 antigen was increased at 7 DPI in lungs of HFHS
200 animals compared to RD animals (median = 2.71 (RD) / 5.043 (HFHS), N = 10 / 4) (**Fig 4 E.J.L**).
201 To confirm this finding, we compared genomic RNA, subgenomic (sg)RNA (surrogate for
202 replicating virus) and infectious viral particles isolated from lungs at 7 DPI. Levels of gRNA and
203 sgRNA in the lungs of HFHS animals at 7 DPI were significantly increased as compared to RD
204 animals. Additionally, no infectious virus could be isolated from a subset of RD animals and
205 overall, significantly more infectious virus could be isolated in HFHS animals (**Fig 4 M.N.O**; RD:
206 N = 10, HFHS: N = 4, gRNA median = 6.935 / 8.513 copies/g lung (\log_{10}), sgRNA median = 5.639
207 / 7.896 copies/g lung (\log_{10}) and infectious virus median = 1.63 / 3.703 TCID₅₀/g (\log_{10}), Mann-
208 Whitney test, p = 0.0240, p = 0.0240 and p = 0.0120, respectively).

209 To better understand if the HFHS diet contributed to changes in viral replication kinetics in the
210 upper respiratory tract, swabs from the oropharynx were analyzed for the presence of sgRNA.
211 Respiratory shedding in both groups peaked at 2 DPI. Shedding in HFHS animals was constantly
212 high up until 10 DPI, while shedding began decreasing in RD animals after 6 DPI. To compare
213 the overall shedding burden, we performed an area under the curve (AUC) analysis for both
214 groups depicting the cumulative shedding. HFHS animals presented significantly higher
215 cumulative shedding (**Fig 4 P.Q**, N = 5 (RD) / 3 (HFHS), median 41.48 / 44.44 AUC (\log_{10}), Mann-
216 Whitney test, p = 0.0357).

217

218

219 **Immune infiltration in the lung during the acute-phase of infection and humoral immunity**
220 **are not significantly affected by high-fat high-sugar diet**

221 Using immunohistochemistry, we investigated the infiltration of macrophages (IBA 1 staining), T-
222 cells (CD3 staining), and B-cells (Pax 5 staining) over the course of infection (**Fig 5**). Macrophages
223 were detected throughout all sections but were increased in 7 and 14 DPI samples in pneumonic
224 areas irrespective of diet regimen. In addition, T lymphocytes were increased in 7 and 14 DPI
225 samples in pneumonic areas. No increase in B cells was observed. To quantify the influx of
226 macrophages and T cells we used morphometric analysis (**Sup Fig 5**). No significant difference
227 was seen between the RD and HFHS groups. Both macrophages and T cells increased in
228 numbers at 7 DPI as compared to pre-challenge conditions for both groups. (**Fig 6 A,B**, pre-
229 challenge: N = (RD) / 2 (HFHS) and 7 DPI: N = 10 (RD) / 4 (HFHS), median macrophages =
230 (3.075 / 3.530 (pre-challenge)) / (13.630 / 10.480 (7 DPI)) % reactivity and median T cells = (4.515
231 / 4.125 (pre-challenge)) / (11.340 / 11.255 (7 DPI)) % reactivity, ordinary two-way ANOVA,
232 followed by Sidak's multiple comparisons test, $p = 0.1007 / 0.3564$ and $p = 0.0001 / 0.0001$,
233 respectively).

234 The humoral response to SARS-CoV-2 was not significantly impacted by diet regimen. Animals
235 seroconverted at 7 DPI, as measured by anti-spike IgG ELISA (**Fig 6 C**, 7 DPI: N = 10 (RD) / 4
236 (HFHS), 14 DPI: N = 5 (RD) / 4 (HFHS), 21 DPI: N = 5 (RD) / 3 (HFHS), ordinary two-way ANOVA,
237 followed by Tukey's multiple comparisons test, $p = 0.8573$, $p = 0.8203$ and $p = 0.5468$,
238 respectively). Neutralization of virus by sera collected at 14 and 21 DPI was compared to assess
239 potential differences in affinity maturation and no significant difference was found (**Fig 6 D**, 14
240 DPI: N = 5 (RD) / 4 (HFHS), 21 DPI: N = 5 (RD) / 3 (HFHS), 14 DPI median = 120 / 80 and 21
241 DPI median = 120/120 reciprocal titer, ordinary two-way ANOVA, followed by Tukey's multiple
242 comparisons test, $p = 0.5535$ and $p = 0.4688$, respectively).

243

244 **Prolonged SARS-CoV-2 shedding, systemic immune and metabolomic dysregulation after**
245 **high-fat high-sugar diet**

246 The cytokine kinetics were analyzed in serum throughout the course of infection by ELISA. Serum
247 samples were collected pre-challenge (0 DPI), on 7 DPI, 14 DPI and 21 DPI (**Fig 6 E**). Pro-
248 inflammatory tumor necrosis factor (TNF)- α , interleukin (IL)-6, antiviral interferon (IFN)- γ , and (IL)-
249 10 did not significantly differ between diet regimens pre-challenge. After infection, RD animals
250 mounted a significant IFN- γ response which lasted into recovery (14 and 21 DPI), while no
251 response was seen in HFHS animals (RD: N = 5/10, HFHS: N = 4, pre-challenge median = 629 /
252 618, 7 DPI median = 737.85 / 550.6, 14 DPI median = 702.3 / 623.55, 21 DPI median = 1042.3 /
253 609.8 pg/mL, ordinary two-way ANOVA, followed by Sidak's multiple comparisons test, pre-
254 challenge: p = 0.58157, 7 DPI: p = 0.0090, 14 DPI: p = 0.7373, 21 DPI p < 0.0001). In contrast,
255 serum IL-6 trended higher in HFHS animals compared to RD animals at 7 DPI (median = 2795.5
256 (RD) / 2859.2 (HFHS) pg/mL). This trend toward higher IL-6 continued at 14 and 21 DPI. IL-10
257 levels trended higher in HFHS animals during the acute phase and remained elevated at 14 DPI
258 (RD: N = 5/10, HFHS: N = 4, pre-challenge median = 1894.6 / 2131.5, 7 DPI median = 2071.75 /
259 2773.95, 14 DPI median = 1768.5 / 2354.35, 21 DPI median = 1733.7 / 2407.6 pg/mL ordinary
260 two-way ANOVA, followed by Sidak's multiple comparisons test, pre-challenge: p = 0.9933, 7 DPI:
261 p = 0.0548, 14 DPI: p = 0.1408, 21 DPI p = 1259). TNF- α serum levels demonstrated an
262 ambivalent pattern.

263 To examine compositional changes in the circulating lipidome over the course of infection, the
264 lipidome was analyzed between 0 DPI and 7 DPI of infection. This analysis revealed distinct lipid
265 dynamics in response to SARS-CoV-2 infection (**Fig 6 F**). RD animals displayed a serum lipid
266 shift in response to infection consisting primarily of decreased levels of phospholipids with mixed
267 representation of lipid classes and a distribution of long chain and polyunsaturated fatty acids
268 (PUFA). HFHS serum displayed a more drastic pattern of lipid depletion and enrichment.

269 Specifically, HFHS serum reflected a sharp enrichment of free polyunsaturated fatty acids (PUFA)
270 and a combination of enrichment and depletion of PUFA containing phospholipids. This response
271 peaked at 7 DPI and began to return to homeostasis by 14 DPI, though certain lipid patterns were
272 carried out until 21 DPI.

273

274 **Discussion**

275 The development of animal models that faithfully recapitulate certain aspects of human disease
276 remains a top priority in SARS-CoV-2 research. Healthy Syrian hamsters develop mild to
277 moderate disease similar to the majority of human cases; however, they do not exhibit the more
278 severe respiratory disease seen in humans with comorbidities such as obesity, diabetes, or other
279 chronic illness (Araújo et al., 2019; Hussain et al., 2020; Korakas et al., 2020). Thus, we
280 developed an experimental infection model of hamsters exclusively fed a high-fat high-sugar diet
281 to model the impact of Western Diet on COVID-19 severity. In the Syrian hamster, this diet caused
282 diet-induced morbidity, led to increased weight gain during adolescence, and ultimately led to in
283 increased glucose tolerance, systemic hyperlipidemia, increased total cholesterol and a liver
284 pathology reminiscent of a NAFLD-like phenotype. The lack of net weight gain in this model may
285 present a means of decoupling liver associated pathologies such as NAFLD from obesity-
286 associated disease more broadly. In humans NAFLD is predominantly a consequence of obesity
287 and frequently associated also with other comorbidities as well (Sanyal, 2019). In the context of
288 COVID-19, NAFLD is associated with increased hospitalization and disease severity (Bramante
289 et al., 2020).

290 The morbidity observed in the absence of infection in the HFHS group should be considered in
291 future studies utilizing this model. In particular, this feature of the model may make survival-based
292 studies difficult. Human clinical studies of COVID-19 are plagued by this same difficulty in
293 quantifying the contribution of infection and the associated comorbidities to the eventual cause of
294 death. If appropriately controlled for in this model the relative contribution to death from the

295 infection and the comorbidities can be quantified. We observed that male hamsters on a HFHS
296 diet demonstrated delayed lower and upper respiratory tract clearance after infection with SARS-
297 CoV-2, which was accompanied by more severe disease presentation. Our data is in agreement
298 with findings in mice, which have reported enhanced morbidity in aged and diabetic obese mice
299 in a mouse-adapted SARS-CoV-2 model (Rathnasinghe et al., 2021). Conversely, we also
300 observed increased weight loss, pathology, delayed lung recovery and influx of immune cells into
301 the lung in a subset of hamsters fed a regular diet as compared to what has been shown in
302 younger animals (Chan et al., 2020; Rosenke et al., 2020). This is likely due to the increased age
303 of the animals used in this study (Osterrieder et al., 2020). Previously, lung function analysis after
304 SARS-CoV-2 infection in a rodent model has only been demonstrated in ACE2 mice (Winkler et
305 al., 2020). While not significantly different between the diet groups, we performed functional lung
306 analysis for the first time in the Syrian hamster after SARS-CoV-2 infection and demonstrated
307 that this model also recapitulates increased total airway resistance and decreased inspiratory
308 capacity. This suggests that the Syrian hamster, besides recapitulating lung pathology, may also
309 be a useful model for mechanistic studies of the respiratory parameters affected by COVID-19.
310 Importantly, the HFHS Syrian hamster model presented here recapitulated two key mediators of
311 severe human COVID-19. One unique feature of the cytokine profile in human disease is the
312 elevation of IL-6 and IL-10, which have been indicated as causes of increased pathology (Chen
313 et al., 2020; Dhar et al., 2020; Lu et al., 2021; Wang et al., 2020). In line with this, in HFHS animals
314 we observed trending increases in serum IL-10 and IL-6 levels after infection. Secondly, in
315 response to infection, HFHS animals showed a more severe response in their serum lipids at 7
316 DPI compared to RD animals. The lipids that dominated this response were free-PUFAs and
317 PUFA-containing phosphatidylethanolamine (PE). In addition, we saw mixed increase and
318 decrease of PUFA-containing plasmalogens and triacylglycerols. The metabolic comorbidities
319 associated with severe COVID-19 were previously shown to correlate with specific mobilization
320 of serum lipids in a human cohort (Schwarz et al., 2020). Specifically, disease severity, defined

321 by ICU admittance, was shown to be associated with increased free PUFAs and PUFA-containing
322 phosphatidylethanolamine, as well as a decrease of PUFA-containing phosphatidylcholine and
323 plasmalogen, compared to non-ICU hospitalized patients. These imbalances were reflected in the
324 circulating milieu of immune-active, PUFA-derived lipid mediators in these patients. The lipid
325 pattern findings in the Syrian hamster model suggest that these serum lipid changes are
326 dependent on preexisting serum hyperlipidemia and stimulated by infection with SARS-CoV-2.
327 Despite the lack of obesity in these animals, the matching of clinical SARS-CoV-2-associated lipid
328 patterns and cytokine profile in this model supports its utility in examining lipid and inflammation
329 dynamics associated immune dysregulation during infection.

330 Of note, this did not seem to adversely affect the humoral immune response while viral titers in
331 oropharyngeal swabs and lung tissues suggested delayed clearance in the HFHS group. This
332 may indicate that other immune pathways were disproportionately affected, but further
333 investigations would be necessary to draw concrete conclusions.

334 Taking the limitations of the model into account, our data further suggests the possible suitability
335 of the Syrian hamster model to assess immunomodulatory therapies. While dietary advice for
336 those suffering from metabolic diseases is proposed to reduce burden of severe COVID-19
337 (Demasi, 2021), it remains doubtful if any change in diet can impact disease outcome favorably
338 after infection has occurred. Targeted immunomodulatory therapies, such as anti-IL-6 therapies,
339 may be more efficient (Zhong et al., 2020). The Syrian hamster model may also be applied to
340 further studies of selected aspects of NAFLD, which the model recapitulates. This model seems
341 to present with an absence or limited amount of liver fibrosis; further work is needed to
342 demonstrate how faithfully it assesses the direct effect of liver fibrosis on acute disease. However,
343 it may be useful to assess long term post-COVID-19 NAFLD, to document further deterioration of
344 liver damage (Portincasa et al., 2020) and the relation to infection sequelae.

345

346 **Acknowledgements**

347 The authors would like to thank Kwe Claude Yinda and Robert Fisher for technical support, the
348 Rocky Mountain Veterinary branch, including Marissa Woods, Nicki Arndt, Amanda Weidow,
349 Linda Couey and Brian Mosbrucker for assistance with high containment husbandry, Tina
350 Thomas, and Rebecca Rosenke for assistance with histology and Danielle Hopkins for flexiVent
351 support and Kathryn Willebrand and Taylor Saturday for assistance with manuscript editing. This
352 research was supported by the Intramural Research Program of the National Institute of Allergy
353 and Infectious Diseases (NIAID), National Institutes of Health (NIH).

354

355 **Author Contributions**

356 Conceptualization, J.R.P.;
357 Methodology, J.R.P., D.R.A., and B.S.;
358 Investigation, J.R.P., D.R.A., B.S., J.E.S., V.A.A., M.G.H., J.N.P., D.S, K.A.S., I.L., B.J.S., C.S.;
359 Writing – Original Draft, J.R.P., D.R.A., B.S., C.S.;
360 Writing – Review & Editing, J.R.P., D.R.A. and V.J.M.;
361 Funding Acquisition, VJ..M.;
362 Resources, V.A.A., B.S., B.J.S. and C.M.B.;
363 Supervision, V.J.M.

364

365

366 **Declaration of Interest**

367 The authors declare no competing financial interests.

368

369 **Methods**

370 *Ethics statement*

371 Approval of animal experiments was obtained from the Institutional Animal Care and Use
372 Committee of the Rocky Mountain Laboratories. Performance of experiments was done following
373 the guidelines and basic principles in the United States Public Health Service Policy on Humane
374 Care and Use of Laboratory Animals and the Guide for the Care and Use of Laboratory Animals.
375 Work with infectious SARS-CoV-2 strains under BSL3 conditions was approved by the
376 Institutional Biosafety Committee (IBC). Inactivation and removal of samples from high

377 containment was performed per IBC-approved standard operating procedures (Haddock et al.,
378 2021).

379

380 *Virus and cells*

381 SARS-CoV-2 strain nCoV-WA1-2020 (MN985325.1) was provided by CDC, Atlanta, USA. Virus
382 propagation was performed in VeroE6 cells in DMEM supplemented with 2% foetal bovine serum
383 (FBS), 2 mM L-glutamine, 100 U/mL penicillin and 100 µg/mL streptomycin. VeroE6 cells were
384 maintained in DMEM supplemented with 10% FBS, 2 mM L-glutamine, 100 U/mL penicillin and
385 100 µg/mL streptomycin D10. Virus stock was 100% identical to the initial sequence
386 (MN985325.1) and no contaminants were detected.

387

388 *High-fat high-sugar diet*

389 Four to six-week-old male Syrian Golden hamsters (ENVIGO) were randomly assigned to either
390 regular rodent chow (Teklad Global 16% Protein Rodent Diet, Envigo) or a HFHS diet for 16
391 weeks (Purina Chow #5001 with 11.5% Corn Oil, 11.5% Coconut Oil, 0.5% Cholesterol, 0.25%
392 Deoxycholic Acid, and 10% Fructose: Dyets Inc., Dyet#615088). Pre-challenge oral glucose tests
393 were performed on all animals. Five animals from each diet group were euthanized after the 16
394 wks for collection of pre-challenge tissue samples and weights. For each diet group, 5 animals
395 were randomly designated for flexiVent calibration and excluded from further analysis. Three
396 animals in the HFHS regimen were euthanized throughout the 16-week diet regimen due to
397 secondary morbidities and were not included in analyses. Pre-challenge, an additional 5 animals
398 in the RD group and additional 8 animals in the HFHS group were excluded from the study due
399 to experimental reasons, and one animal in the HFHS group due to secondary morbidities.

400

401 *Assessment of glucose tolerance*

402 An oral glucose tolerance test (OGTT) was performed after 16 weeks of diet manipulation
403 (Dalbøge et al., 2015). Hamsters were fasted for 16 h overnight preceding the OGTT. An oral
404 glucose load (2 g/kg glucose) was administered. Blood samples were collected from the
405 retroorbital sinus using capillary tube at 0-, 30-, 60-, and 120-min post glucose administration.
406 Blood glucose was measured using the AlphaTRAK blood glucose monitoring system (Zoetis),
407 calibrated for cats. Serum was separated and used for measurement of insulin. Insulin was
408 measured using the rat/mouse insulin ELISA kit from Millipore (EZRMI-13K), according to the
409 manufacturer's instructions (Wang et al., 2001).

410

411 *Lipidomics*

412 Blood lipids were assessed for a subset of animals (N= 8-10) after 16 weeks of diet. 200 µL blood
413 was collected and were measured using the Piccolo® Lipid Panel Plus for humans (Abraxis)
414 according to the manufacturer's instruction.

415

416 *Next-generation sequencing of liver mRNA*

417 Frozen tissues were pulverized in 1 mL of Trizol (ThermoFisher Scientific), 200 µL of 1-Bromo-3-
418 chloropropane (MilliporeSigma) was added, samples mixed, and centrifuged at 16,000 x g for 15
419 min at 4 °C. RNA containing aqueous phase of 600 µL was collected from each sample and
420 passed through Qias shredder column (Qiagen) at 21,000 x g for 2 min to homogenize any
421 remaining genomic DNA in the aqueous phase. Aqueous phase was combined with 600 µL of
422 RLT lysis buffer (Qiagen, Valencia, CA) with 1% beta mercaptoethanol (MilliporeSigma) and RNA
423 was extracted using Qiagen AllPrep DNA/RNA 96-well system. An additional on-column DNase-
424 1 treatment was performed during RNA extraction. RNA was quantitated by spectrophotometry
425 and yield ranged from 0.4 to 17.8 µg. One hundred nanograms of RNA was used as input for
426 rRNA depletion and NGS library preparation following the Illumina Stranded Total RNA Prep
427 Ligation with Ribo-Zero Plus workflow (Illumina). The NGS libraries were prepared, amplified for

428 13 cycles, AMPureXP bead (Beckman Coulter) purified using 0.95X beads, assessed on a
429 BioAnalyzer DNA1000 chip (Agilent Technologies) and quantified using the Kapa Quantification
430 Kit for Illumina Sequencing (Roche). Amplified libraries were pooled at equal molar amounts and
431 sequenced on a NextSeq (Illumina) using two High Output 150 cycle chemistry kits. Raw fastq
432 reads were trimmed of Illumina adapter sequences using cutadapt version 1.12 and then trimmed
433 and filtered for quality using the FASTX-Toolkit (Hannon Lab). Remaining reads were aligned to
434 the *Mesocricetus auratus* genome assembly version 1.0 using Hisat2 (Kim et al., 2015). Reads
435 mapping to genes were counted using htseq-count (Anders et al., 2015). Differential expression
436 analysis was performed using the Bioconductor package DESeq2 (Love et al., 2014). Pathway
437 analysis was performed using Ingenuity Pathway Analysis (QIAGEN) and gene clustering was
438 performed using Partek Genomics Suite (Partek Inc.). Samples with too low quality were removed
439 from the analysis (Sup Table 1).

440

441 *Next-generation sequencing of virus*

442 For sequencing from viral stocks, sequencing libraries were prepared using Stranded Total RNA
443 Prep Ligation with Ribo-Zero Plus kit per manufacturer's protocol (Illumina) and sequenced on an
444 Illumina MiSeq at 2 x 150 base pair reads. For sequencing from swab and lung tissue, total RNA
445 was depleted of ribosomal RNA using the Ribo-Zero Gold rRNA Removal kit (Illumina).
446 Sequencing libraries were constructed using the KAPA RNA HyperPrep kit following
447 manufacturer's protocol (Roche Sequencing Solutions). To enrich for SARS-CoV-2 sequence,
448 libraries were hybridized to myBaits Expert Virus biotinylated oligonucleotide baits following the
449 manufacturer's manual, version 4.01 (Arbor Biosciences). Enriched libraries were sequenced on
450 the Illumina MiSeq instrument as paired-end 2 X 150 base pair reads. Raw fastq reads were
451 trimmed of Illumina adapter sequences using cutadapt version 1.1227 and then trimmed and
452 filtered for quality using the FASTX-Toolkit (Hannon Lab, CSHL). Remaining reads were mapped
453 to the SARS-CoV-2 2019-nCoV/USA-WA1/2020 genome (MN985325.1) using Bowtie2 version

454 2.2.928 with parameters --local --no-mixed -X 1500. PCR duplicates were removed using picard
455 MarkDuplicates (Broad Institute) and variants were called using GATK HaplotypeCaller version
456 4.1.2.029 with parameter -ploidy 2. Variants were filtered for QUAL > 500 and DP > 20 using
457 bcftools.

458

459 *Inoculation experiments*

460 After 16 weeks, animals were then inoculated intranasally (I.N.) under isoflurane anaesthesia. I.N.
461 inoculation was performed with 40 μ L sterile Dulbecco's Modified Eagle Medium (DMEM)
462 containing 8×10^4 TCID₅₀ SARS-CoV-2. A subset of animals (N= 4-10) were euthanized, and
463 serum and tissues were collected at pre-challenge (0 DPI), 4, 7, 14, and 21 DPI. Hamsters were
464 weighted daily, and oropharyngeal swabs (21 DPI animals only) were taken daily until day 7 and
465 then thrice a week. Swabs were collected in 1 mL DMEM with 200 U/mL penicillin and 200 μ g/mL
466 streptomycin. Hamsters were observed daily for clinical signs of disease.

467

468 *Lung function analyses*

469 Lung function assessment was performed on pre-challenge, 7, 14, and 21 DPI. Hamsters were
470 anesthetized with a combination of inhalant isoflurane and ketamine/xylazine intraperitoneally.
471 After animals reached a surgical plane of anaesthesia a terminal tracheostomy was performed as
472 previously described (McGovern TK JOVE 2013). Briefly, a cannula was introduced into the
473 trachea, secured with suture, and the animal underwent the forced oscillation technique (FOT)
474 using a flexiVent (SCIREZ, Inc.). Animals were kept at a consistent surgical plane of anesthesia
475 to the point of not resisting the FOT procedure. Animals were immediately euthanized while
476 deeply anesthetized after FOT was completed; the surgical procedure was terminal.

477

478 *Histopathology and immunohistochemistry*

479 Necropsies and tissue sampling were performed according to IBC-approved protocols. Tissues
480 were fixed for a minimum of 7 days in 10% neutral buffered formalin with 2 changes. Tissues were
481 placed in cassettes and processed with a Sakura VIP-6 Tissue Tek, on a 12-hour automated
482 schedule, using a graded series of ethanol, xylene, and ParaPlast Extra. Prior to staining,
483 embedded tissues were sectioned at 5 μm and dried overnight at 42°C. Using GenScript
484 U864YFA140-4/CB2093 NP-1 (1:1000) specific anti-CoV immunoreactivity, CD3 (Predilute)
485 (Roche Tissue Diagnostics #790-4341), and PAX5 (1:500) (Novus Biologicals #NBP2-38790)
486 were detected using the Vector Laboratories ImPress VR anti-rabbit IgG polymer (# MP-6401) as
487 the secondary antibody. Iba-1 (1:500) (abcam #ab5076) was detected using Roche Tissue
488 Diagnostics OmniMap anti-goat multimer (#760-4647) as the secondary antibody. The tissues
489 were stained using the Discovery Ultra automated stainer (Ventana Medical Systems) with a
490 ChromoMap DAB kit Roche Tissue Diagnostics (#760-159).

491

492 *Morphometric analysis.*

493 IHC stained tissue slides were scanned with an Aperio ScanScope XT (Aperio Technologies, Inc.)
494 and analyzed using the ImageScope Positive Pixel Count algorithm (version 9.1). The default
495 parameters of the Positive Pixel Count (hue of 0.1 and width of 0.5) detected antigen adequately.

496

497 *Viral RNA detection*

498 Swabs from hamsters were collected as described above. Cage and bedding material was
499 sampled with prewetted swabs in 1 mL of DMEM supplemented with 200 U/mL penicillin and 200
500 $\mu\text{g}/\text{mL}$ streptomycin. Then, 140 μL was utilized for RNA extraction using the QIAamp Viral RNA
501 Kit (Qiagen) using QIAcube HT automated system (Qiagen) according to the manufacturer's
502 instructions with an elution volume of 150 μL . Sub-genomic (sg) viral RNA and genomic (g) was
503 detected by qRT-PCR (Corman et al., 2020a; Corman et al., 2020b). Five μL RNA was tested
504 with TaqMan™ Fast Virus One-Step Master Mix (Applied Biosystems) using QuantStudio 6 Flex

505 Real-Time PCR System (Applied Biosystems) according to instructions of the manufacturer. Ten-
506 fold dilutions of SARS-CoV-2 standards with known copy numbers were used to construct a
507 standard curve and calculate copy numbers/mL.

508

509 *Viral titration*

510 Viable virus in tissue samples was determined as previously described (van Doremalen et al.,
511 2017). In brief, lung tissue samples were weighted, then homogenized in 1 mL of DMEM2. VeroE6
512 cells were inoculated with ten-fold serial dilutions of tissue homogenate, spun at 1000 rpm for 1 h
513 at 37 °C, the first dilutions washed with PBS and with DMEM2. Cells were incubated with tissue
514 homogenate for 6 days at 37 °C, 5% CO₂, then scored for cytopathic effect. TCID₅₀ was calculated
515 by the method of Spearman-Kärber and adjusted for tissue weight.

516

517 *Serology*

518 Serum samples were inactivated with γ -irradiation (2 mRad) and analyzed as previously
519 described (Yinda et al., 2020). In brief, maxisorp plates (Nunc) were coated with 50 ng spike
520 protein (generated in-house) per well and incubated overnight at 4 °C. After blocking with casein
521 in phosphate buffered saline (PBS) (ThermoFisher) for 1 h at room temperature (RT), serially
522 diluted 2-fold serum samples (duplicate, in blocking buffer) were incubated for 1 h at RT. Spike-
523 specific antibodies were detected with goat anti-hamster IgG Fc (horseradish peroxidase (HRP)-
524 conjugated, Abcam) for 1 h at RT and visualized with KPL TMB 2-component peroxidase
525 substrate kit (SeraCare, 5120-0047). The reaction was stopped with KPL stop solution (Seracare)
526 and read at 450 nm. Plates were washed 3 to 5 x with PBS-T (0.1 % Tween) for each wash. The
527 threshold for positivity was calculated as the average plus 3 x the standard deviation of negative
528 control hamster sera.

529

530 *Cytokine analysis*

531 Cytokine concentrations were determined using a commercial hamster ELISA kit for TNF- α , INF-
532 γ , IL-6, IL-4, and IL-10 available at antibodies.com, according to the manufacturer's instructions
533 (antibodies.com; A74292, A74590, A74291, A74027, A75096). Samples were pre-diluted 1:10.

534

535 Serum lipid analysis

536 For abundance analysis of serum lipids signals were filtered using a 50 % miss value cut off and
537 applying a raw intensity cutoff appropriate to the noise level of each class of lipids. Signals were
538 then normalized to internal deuterated SPLASH® LIPIDOMIX® Mass Spec Standard (Avanti
539 Polar Lipids). For compositional analysis of the serum, bulk lipid datasets were further filtered
540 using a 30 % QC coefficient of variance cut off prior to normalizing by the total signal sum. All
541 univariate and multivariate analysis was performed using GraphPad Prism or MarkerView (AB
542 Sciex). All parallel univariate analysis was subjected to a Benjamini-Hochberg correction using a
543 false discovery rate of 15 %.

544

545 *Statistical analysis*

546 All graphs were designed in GraphPad Prism software (version 8.0.1; GraphPad Software).
547 Significance test were performed as indicated where appropriate. Statistical significance levels
548 were determined as follows: ns = $p > 0.05$; * = $p \leq 0.05$; ** = $p \leq 0.01$; *** = $p \leq 0.001$; **** = $p \leq$
549 0.0001.

550

551

552

553 **References**

554

555 Anders, S., Pyl, P.T., and Huber, W. (2015). HTSeq--a Python framework to work with high-throughput
556 sequencing data. *Bioinformatics* 31, 166-169.

557 Araújo, J., Cai, J., and Stevens, J. (2019). Prevalence of Optimal Metabolic Health in American Adults:
558 National Health and Nutrition Examination Survey 2009-2016. *Metab Syndr Relat Disord* 17, 46-52.

559 Bramante, C., Tignanelli, C.J., Dutta, N., Jones, E., Tamariz, L., Clark, J.M., Usher, M., Metlon-Meaux,
560 G., and Ikramuddin, S. (2020). Non-alcoholic fatty liver disease (NAFLD) and risk of hospitalization for
561 Covid-19. medRxiv.

562 Butler, M.J., and Barrientos, R.M. (2020). The impact of nutrition on COVID-19 susceptibility and long-
563 term consequences. *Brain Behav Immun* 87, 53-54.

564 Cefalu, W.T., and Rodgers, G.P. (2021). COVID-19 and metabolic diseases: a heightened awareness of
565 health inequities and a renewed focus for research priorities. *Cell Metabolism* 33, 473-478.

566 Chan, J.F.-W., Zhang, A.J., Yuan, S., Poon, V.K.-M., Chan, C.C.-S., Lee, A.C.-Y., Chan, W.-M., Fan, Z.,
567 Tsoi, H.-W., Wen, L., *et al.* (2020). Simulation of the Clinical and Pathological Manifestations of
568 Coronavirus Disease 2019 (COVID-19) in a Golden Syrian Hamster Model: Implications for Disease
569 Pathogenesis and Transmissibility. *Clinical Infectious Diseases*.

570 Chen, G., Wu, D., Guo, W., Cao, Y., Huang, D., Wang, H., Wang, T., Zhang, X., Chen, H., Yu, H., *et al.*
571 (2020). Clinical and immunological features of severe and moderate coronavirus disease 2019. *J Clin*
572 *Invest* 130, 2620-2629.

573 Cordain, L., Eaton, S.B., Sebastian, A., Mann, N., Lindeberg, S., Watkins, B.A., O'Keefe, J.H., and
574 Brand-Miller, J. (2005). Origins and evolution of the Western diet: health implications for the 21st
575 century. *Am J Clin Nutr* 81, 341-354.

576 Corman, V.M., Landt, O., Kaiser, M., Molenkamp, R., Meijer, A., Chu, D.K., Bleicker, T., Brünink, S.,
577 Schneider, J., Schmidt, M.L., *et al.* (2020a). Detection of 2019 novel coronavirus (2019-nCoV) by real-
578 time RT-PCR. *Euro surveillance : bulletin Europeen sur les maladies transmissibles = European*
579 *communicable disease bulletin* 25, 2000045.

580 Corman, V.M., Landt, O., Kaiser, M., Molenkamp, R., Meijer, A., Chu, D.K., Bleicker, T., Brunink, S.,
581 Schneider, J., Schmidt, M.L., *et al.* (2020b). Detection of 2019 novel coronavirus (2019-nCoV) by real-
582 time RT-PCR. *Euro Surveill* 25.

583 Dalbøge, L.S., Pedersen, P.J., Hansen, G., Fabricius, K., Hansen, H.B., Jelsing, J., and Vrang, N. (2015).
584 A Hamster Model of Diet-Induced Obesity for Preclinical Evaluation of Anti-Obesity, Anti-Diabetic and
585 Lipid Modulating Agents. *PloS one* 10, e0135634-e0135634.

586 Demasi, M. (2021). COVID-19 and metabolic syndrome: could diet be the key? *BMJ Evidence-Based*
587 *Medicine* 26, 1-2.

588 Dhar, S.K., K, V., Damodar, S., Gujar, S., and Das, M. (2020). IL-6 and IL-10 as predictors of disease
589 severity in COVID 19 patients: Results from Meta-analysis and Regression. medRxiv,
590 2020.2008.2015.20175844.

591 Green, W.D., and Beck, M.A. (2017a). Obesity altered T cell metabolism and the response to infection.
592 *Curr Opin Immunol* 46, 1-7.

593 Green, W.D., and Beck, M.A. (2017b). Obesity Impairs the Adaptive Immune Response to Influenza
594 Virus. *Ann Am Thorac Soc* 14, S406-s409.

595 Haddock, E., Feldmann, F., Shupert, W.L., and Feldmann, H. (2021). Inactivation of SARS-CoV-2
596 Laboratory Specimens. *Am J Trop Med Hyg* 104, 2195-2198.

597 Hayashi, T., Boyko, E.J., Sato, K.K., McNeely, M.J., Leonetti, D.L., Kahn, S.E., and Fujimoto, W.Y.
598 (2013). Patterns of insulin concentration during the OGTT predict the risk of type 2 diabetes in Japanese
599 Americans. *Diabetes Care* 36, 1229-1235.

600 Hussain, A., Mahawar, K., Xia, Z., Yang, W., and El-Hasani, S. (2020). Obesity and mortality of
601 COVID-19. Meta-analysis. *Obes Res Clin Pract* 14, 295-300.

602 Kasim-Karakas, S.E., Vriend, H., Almario, R., Chow, L.C., and Goodman, M.N. (1996). Effects of
603 dietary carbohydrates on glucose and lipid metabolism in golden Syrian hamsters. *J Lab Clin Med* 128,
604 208-213.

605 Kim, D., Langmead, B., and Salzberg, S.L. (2015). HISAT: a fast spliced aligner with low memory
606 requirements. *Nature Methods* 12, 357-360.

607 Korakas, E., Ikonomidis, I., Kousathana, F., Balampanis, K., Kountouri, A., Raptis, A., Palaiodimou, L.,
608 Kokkinos, A., and Lambadiari, V. (2020). Obesity and COVID-19: immune and metabolic derangement
609 as a possible link to adverse clinical outcomes. *Am J Physiol Endocrinol Metab* 319, E105-e109.
610 Li, G., Liu, X., Zhu, H., Huang, L., Liu, Y., Ma, C., and Qin, C. (2009). Insulin resistance in insulin-
611 resistant and diabetic hamsters (*Mesocricetus auratus*) is associated with abnormal hepatic expression of
612 genes involved in lipid and glucose metabolism. *Comp Med* 59, 449-458.
613 Love, M.I., Huber, W., and Anders, S. (2014). Moderated estimation of fold change and dispersion for
614 RNA-seq data with DESeq2. *Genome Biology* 15, 550.
615 Lu, L., Zhang, H., Dauphars, D.J., and He, Y.-W. (2021). A Potential Role of Interleukin 10 in COVID-
616 19 Pathogenesis. *Trends in Immunology* 42, 3-5.
617 Nie, S., Han, S., Ouyang, H., and Zhang, Z. (2020). Coronavirus Disease 2019-related dyspnea cases
618 difficult to interpret using chest computed tomography. *Respir Med* 167, 105951-105951.
619 Osterrieder, N., Bertzbach, L.D., Dietert, K., Abdelgawad, A., Vladimirova, D., Kunec, D., Hoffmann,
620 D., Beer, M., Gruber, A.D., and Trimpert, J. (2020). Age-Dependent Progression of SARS-CoV-2
621 Infection in Syrian Hamsters. *Viruses* 12.
622 Parry, A.H., Wani, A.H., Yaseen, M., Dar, K.A., Choh, N.A., Khan, N.A., Shah, N.N., and Jehangir, M.
623 (2020). Spectrum of chest computed tomographic (CT) findings in coronavirus disease-19 (COVID-19)
624 patients in India. *Eur J Radiol* 129, 109147-109147.
625 Petrakis, D., Margină, D., Tsarouhas, K., Tekos, F., Stan, M., Nikitovic, D., Kouretas, D., Spandidos,
626 D.A., and Tsatsakis, A. (2020). Obesity - a risk factor for increased COVID-19 prevalence, severity and
627 lethality (Review). *Mol Med Rep* 22, 9-19.
628 Portincasa, P., Krawczyk, M., Smyk, W., Lammert, F., and Di Ciaula, A. (2020). COVID-19 and non-
629 alcoholic fatty liver disease: Two intersecting pandemics. *Eur J Clin Invest* 50, e13338.
630 Rathnasinghe, R., Jangra, S., Cupic, A., Martinez-Romero, C., Mulder, L.C.F., Kehrer, T., Yildiz, S.,
631 Choi, A., Mena, I., De Vrieze, J., *et al.* (2021). The N501Y mutation in SARS-CoV-2 spike leads to
632 morbidity in obese and aged mice and is neutralized by convalescent and post-vaccination human sera.
633 medRxiv, 2021.2001.2019.21249592.
634 Rogero, M.M., and Calder, P.C. (2018). Obesity, Inflammation, Toll-Like Receptor 4 and Fatty Acids.
635 *Nutrients* 10.
636 Rosenke, K., Meade-White, K., Letko, M., Clancy, C., Hansen, F., Liu, Y., Okumura, A., Tang-Huau,
637 T.L., Li, R., Saturday, G., *et al.* (2020). Defining the Syrian hamster as a highly susceptible preclinical
638 model for SARS-CoV-2 infection. *Emerg Microbes Infect*, 1-36.
639 Saklayen, M.G. (2018). The Global Epidemic of the Metabolic Syndrome. *Curr Hypertens Rep* 20, 12.
640 Sanyal, A.J. (2019). Past, present and future perspectives in nonalcoholic fatty liver disease. *Nature*
641 *Reviews Gastroenterology & Hepatology* 16, 377-386.
642 Schwarz, B., Sharma, L., Roberts, L., Peng, X., Bermejo, S., Leighton, I., Casanovas-Massana, A.,
643 Minasyan, M., Farhadian, S., Ko, A.I., *et al.* (2020). Cutting Edge: Severe SARS-CoV-2 Infection in
644 Humans Is Defined by a Shift in the Serum Lipidome, Resulting in Dysregulation of Eicosanoid Immune
645 Mediators. *The Journal of Immunology*, ji2001025.
646 Sia, S.F., Yan, L.M., Chin, A.W.H., Fung, K., Choy, K.T., Wong, A.Y.L., Kaewpreedee, P., Perera, R.,
647 Poon, L.L.M., Nicholls, J.M., *et al.* (2020). Pathogenesis and transmission of SARS-CoV-2 in golden
648 hamsters. *Nature*.
649 Swinburn, B.A., Sacks, G., Hall, K.D., McPherson, K., Finegood, D.T., Moodie, M.L., and Gortmaker,
650 S.L. (2011). The global obesity pandemic: shaped by global drivers and local environments. *The Lancet*
651 378, 804-814.
652 van Doremalen, N., Falzarano, D., Ying, T., de Wit, E., Bushmaker, T., Feldmann, F., Okumura, A.,
653 Wang, Y., Scott, D.P., Hanley, P.W., *et al.* (2017). Efficacy of antibody-based therapies against Middle
654 East respiratory syndrome coronavirus (MERS-CoV) in common marmosets. *Antiviral Res* 143, 30-37.
655 Wang, J., Jiang, M., Chen, X., and Montaner, L.J. (2020). Cytokine storm and leukocyte changes in mild
656 versus severe SARS-CoV-2 infection: Review of 3939 COVID-19 patients in China and emerging
657 pathogenesis and therapy concepts. *J Leukoc Biol*.

658 Wang, P.-R., Guo, Q., Ippolito, M., Wu, M., Milot, D., Ventre, J., Doebber, T., Wright, S.D., and Chao,
659 Y.-S. (2001). High fat fed hamster, a unique animal model for treatment of diabetic dyslipidemia with
660 peroxisome proliferator activated receptor alpha selective agonists. *European Journal of Pharmacology*
661 *427*, 285-293.
662 Washington, I.M., and Van Hoosier, G. (2012). *Clinical Biochemistry and Hematology. The Laboratory*
663 *Rabbit, Guinea Pig, Hamster, and Other Rodents*, 57-116.
664 Winkler, E.S., Bailey, A.L., Kafai, N.M., Nair, S., McCune, B.T., Yu, J., Fox, J.M., Chen, R.E., Earnest,
665 J.T., Keeler, S.P., *et al.* (2020). SARS-CoV-2 infection of human ACE2-transgenic mice causes severe
666 lung inflammation and impaired function. *Nature Immunology* *21*, 1327-1335.
667 Yinda, C.K., Port, J.R., Bushmaker, T., Owusu, I.O., Avanzato, V.A., Fischer, R.J., Schulz, J.E.,
668 Holbrook, M.G., Hebner, M.J., Rosenke, R., *et al.* (2020). K18-hACE2 mice develop respiratory disease
669 resembling severe COVID-19. *bioRxiv*.
670 Zhong, J., Tang, J., Ye, C., and Dong, L. (2020). The immunology of COVID-19: is immune modulation
671 an option for treatment? *The Lancet Rheumatology* *2*, e428-e436.
672

673

674

675 **Figure titles and legend**

676

677 **Figure 1: High-fat and high-sugar diet induces metabolic changes characterized by**
678 **increased juvenile weight gain and glucose tolerance.** Male Syrian hamsters were fed either
679 a regular or high-fat high-sugar diet *ad libitum* for 16 weeks. **A.** Relative weight gain in hamsters
680 on each diet regimen, measured weekly. Graphs show median \pm 95% CI, N = 35, ordinary two-
681 way ANOVA, followed by Sidak's multiple comparisons test. **B.** Oral glucose tolerance test
682 performed at 16 weeks. Graphs show median \pm 95% CI, N = 30 (RD) / 29 (HFHS), ordinary two-
683 way ANOVA, followed by Sidak's multiple comparisons test. **C.** Insulin response after application
684 of oral glucose load as shown by insulin resistance index (fasting glucose level (mmol/L) x fasting
685 insulin level (mIU/L)). Truncated violin plots depicting median, quartiles and individuals, N = 30
686 (RD) / 29 (HFHS), Mann-Whitney test. **D.** Adiposity index as measured by testicular fat pads/total
687 body weight at 16 weeks. Truncated violin plots depicting median, quartiles and individuals, N =
688 5, Mann-Whitney test. **E.** Blood lipid ALT and cholesterol levels measured on a commercially
689 available lipid panel on an automated blood chemistry analyzer. **F.** Serum aggregate lipids signal
690 analyzed by liquid chromatography tandem mass spectrometry (LC-MS/MS) at 16 weeks of diet

691 regimen. Truncated violin plots depicting median, quartiles and individuals, $N = 5(\text{RD}) / 4 (\text{HFHS})$,
692 Mann-Whitney test. Abbreviations: RD = regular diet, HFHS = high-fat high-sugar, ALT = alanine
693 aminotransaminase. p-values are indicated where appropriate.

694
695 **Figure 2. High-fat and high-sugar diet induces liver damage and systemic hyperlipidemia.**

696 Male Syrian hamsters were fed either a regular or high-fat high-sugar diet *ad libitum* and 5 animals
697 from each group were sacrificed week 16 for analyses of liver tissue. **A.D.** Gross imaging of a
698 representative liver from one hamster on the RD and one hamster on the HFHS diet regimen.
699 **B.E.** 20x photomicrograph of H&E-stained slide. **C.F.** 400x photomicrograph of H&E-stained slide.
700 **G.** RNA was isolated for gene expression analyses from liver tissue at 16 weeks. Using Integrated
701 Pathway Analysis (Qiagen), significantly up-regulated canonical pathways were identified.
702 Graphs show pathways associated with cell recruitment, activation, and immunological
703 inflammation ($p > 0.05$, z-score < -2 or > 2). **H.** Integrated Pathway Analysis (Qiagen) was used
704 to depict the gene network associated with nonalcoholic steatohepatitis. Symbols refer to legend
705 below figure. Red: Gene upregulation in high-fat high-sugar animals as compared to regular diet
706 animals. Green: downregulation in comparison to regular diet.

707
708 **Figure 3: High-fat and high-sugar diet exasperated disease severity after SARS-COV-2**

709 **infection.** Male Syrian hamsters were fed either a regular or high-fat high-sugar diet *ad libitum*
710 for 16 weeks, then challenged with 8×10^4 TCID₅₀ SARS-CoV-2. **A.** Survival after challenge for RD
711 ($N = 10$) and HFHS ($N = 9$) in the 14 and 21 DPI groups **B.** Relative weight loss in hamsters after
712 challenge. Left graph shows median \pm 95% CI. Right graph shows area under the curve (AUC,
713 negative peaks only) between 1-14 DPI of surviving animals. Truncated violin plots depicting
714 median, quartiles and individuals, $N = 10 (\text{RD}) / 7 (\text{HFHS})$, Mann-Whitney test. **C.** Lung function
715 analysis after challenge **D.** Pressure-volume loops at pre-challenge, 7, 14, and 21 DPI.
716 Abbreviations: RD = regular diet, HFHS = high-fat high-sugar, DPI = days post inoculation. p-
717 values are indicated where appropriate.

718
719 **Figure 4. High-fat and high-sugar diet is associated to increased pulmonary pathology and**
720 **decreased viral clearance.** Animals were euthanized at 7 DPI with SARS-CoV-2 in order to
721 compare lung pathology and viral titers. **A-J.** Gross and photomicrographic images of hamster
722 lungs taken at 7 DPI. **A, F.** Gross necropsy findings consisted of multifocal well-circumscribed
723 dark red foci throughout turgid lobes which failed to collapse. **B, G.** Dark red foci in the gross
724 images correlate with the consolidated foci adjacent to airways and scattered along the pleural
725 margin in the sub-gross images. HE, 1.4x. **C, H.** Foci of interstitial pneumonia adjacent to terminal
726 bronchioles and accompanying blood vessels. HE, 20x. **D, I.** Pneumonia consists of alveoli
727 containing neutrophils, eosinophils, alveolar and septal macrophages, fibrin, edema and septa
728 lined by hyperplastic type II pneumocytes, HE 400x. Syncytial cells are common (see inset, HE,
729 1000x). Pneumonic areas in the HFHS diet hamsters frequently had abundant intra-alveolar
730 edema (*) and organizing fibrin mixed with inflammatory cells. Note the vessel wall disrupted by
731 sub-endothelial leukocytes and cellular debris (←). **E, J.** anti-SARS-CoV-2 immunoreactivity in
732 the lungs from the regular diet hamsters is rare compared to the frequent pneumocyte
733 immunoreactivity in the lungs of the HFHS diet hamsters, IHC, 400x. **K.** Individual pathological
734 scores. **L.** Quantitative count of SARS-CoV-2 immunoreactivity by morphometric analysis.
735 Truncated violin plots depicting median, quartiles and individuals, N = 10 (RD) / 4 (HFHS), Mann-
736 Whitney test. **M.N.** Lung viral load measured by g and sgRNA. Truncated violin plots depicting
737 median, quartiles and individuals, N = 10 (RD) / 4 (HFHS), Mann-Whitney test. **O.** Infectious virus
738 measured by lung titration. Truncated violin plots depicting median, quartiles and individuals, N =
739 10 (RD) / 4 (HFHS), Mann-Whitney test. Dotted line = limit of detection. Abbreviations: g =
740 genomic, sg = subgenomic, DPI = days post inoculation, H&E = hematoxylin and eosin stain, IHC
741 = immunohistochemistry. p-values are indicated were appropriate.

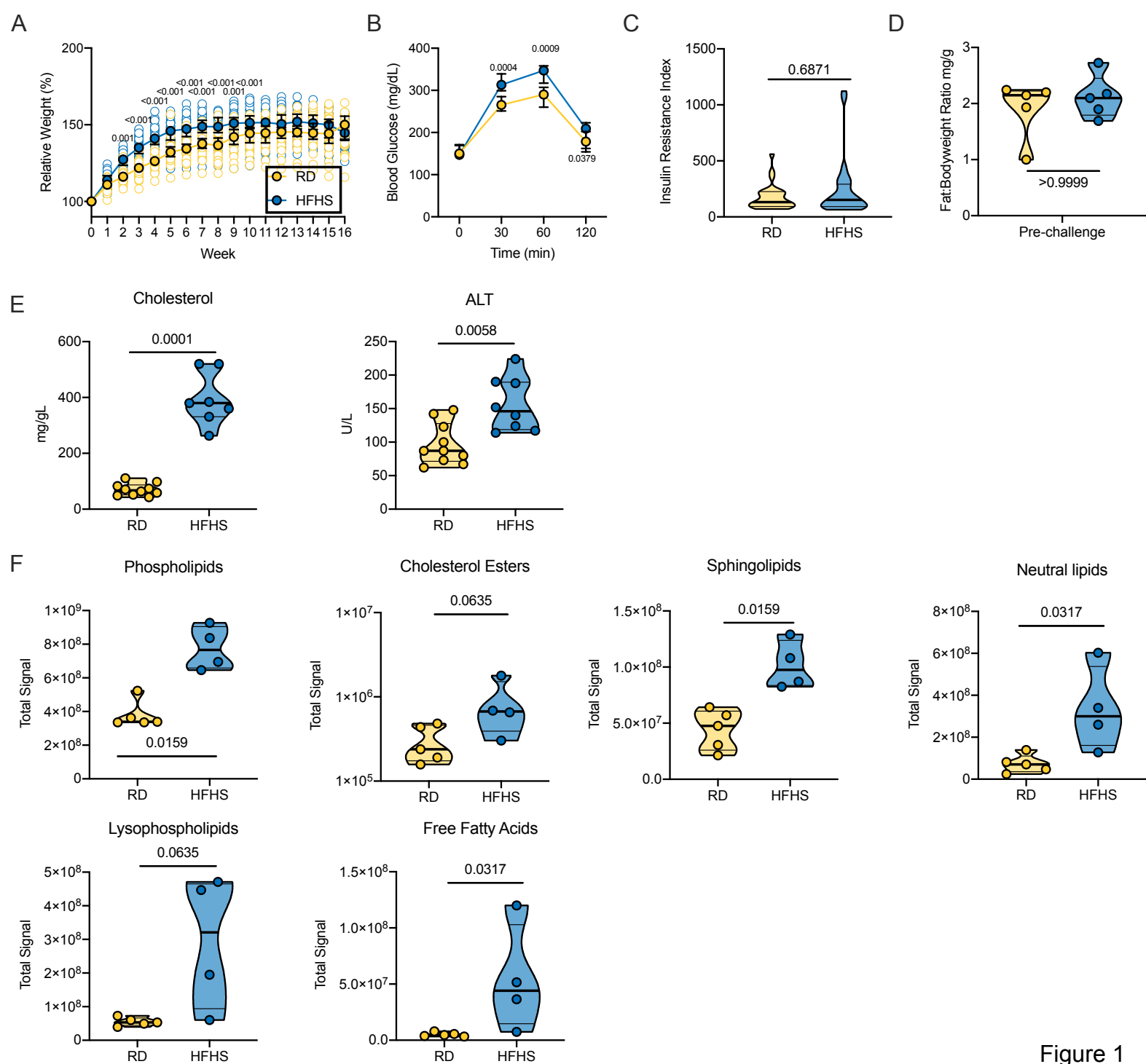
742
743 **Figure 5. Immune infiltration and in the lung during acute-phase of infection and humoral**
744 **immunity is not significantly affected by high-fat high-sugar diet.** Animals were euthanized

745 at 0, 7 and 14 DPI and the presence of SARS-CoV-2 antigen, T-cells, B-cells and macrophages
746 investigated. **A, B.** Pre-challenge RD and HFHS diet hamster lungs. **G, H.** IBA1; **M, N.** CD3 and
747 **S, T.** Pax5. **C, D.** Lungs at 7 DPI. **I, J.** IBA1; **O, P.** CD3 and **U, V** Pax 5. **E, F.** Lungs at 14 DPI.
748 **K, L.** IBA1; **Q, R.** CD3 and **W, X.** Pax 5. **A-F** HE. All images 200x. Abbreviations: RD = regular
749 diet, HFHS = high-fat high-sugar, DPI = days post inoculation.

750

751 **Figure 6. Disease manifestation is accompanied by prolonged viral shedding, systemic**
752 **immune and metabolomic dysregulation after high-fat high-sugar diet.** Animals were
753 euthanized pre-challenge, at 7, 14, and 21 DPI with SARS-CoV-2 and serum and lung tissue
754 collected for immune and lipid mediator analyses. Oropharyngeal swabs were taken to assess
755 respiratory shedding **A.B.** Lung infiltration of T-cells (CD3) and macrophages (IBA1) was
756 quantified by morphometric analysis. Truncated violin plots depicting median, quartiles and
757 individuals, pre-challenge and 14 DPI: N = 2, 7 DPI: N = 10 (RD) / 4 (HFHS), ordinary two-way
758 ANOVA, followed by Turkey's multiple comparisons test. **C.** ELISA titers against spike protein of
759 SARS-CoV-2 (lineage A) in serum obtained pre-challenge, at 7, 14, and 21 DPI. Truncated violin
760 plots depicting median, quartiles and individuals, pre-challenge and 14 DPI: N = 5 (RD) / 4
761 (HFHS), 7 DPI: N = 10 (RD) / 4 (HFHS), 21 DPI: N = 5 (RD) / 3 (HFHS), ordinary two-way ANOVA,
762 followed by Sidak's multiple comparisons test. **D.** Virus neutralization titers against SARS-CoV-2
763 (lineage A) in serum obtained at 14 and 21 DPI. Truncated violin plots depicting median quartiles
764 and individuals, 14 DPI: N = 5 (RD) / 4 (HFHS), 21 DPI: N = 5 (RD) / 3 (HFHS), ordinary two-way
765 ANOVA, followed by Sidak's multiple comparisons test. **E.F.** Viral load in oropharyngeal swabs
766 measured in sgRNA copy number for RD and HFHS animals. Graphs show median, individual
767 animals and 95% CI (shaded area). Dotted line = peak shedding. **G.** Area under the curve (AUC)
768 analysis of virus shedding shown in E/F. Truncated violin plots depicting median quartiles and
769 individuals, 21 DPI: N = 5 (RD) / 3 (HFHS), Mann-Whitney test. **H.** Serum levels (pg/mL) of INF-
770 γ , TNF α -, IL-6 and IL-10 measured by ELISA from serum collected on 0, 7, 14, and 21 DPI.

771 Truncated violin plots depicting median quartiles and individuals, pre-challenge/14 and 21 DPI: N
772 = 5 (RD) / 4 (HFHS), 7 DPI: N = 10 (RD) / 4 (HFHS), ordinary two-way ANOVA, followed by
773 Sidak's multiple comparisons test. I. Lipid time-course heatmap: Changes in PUFA-containing
774 serum lipids associated with an active SARS-CoV-2 infection as measured by LC-MS/MS.
775 Autoscaled intensities are displayed for serum lipids species that were significantly changed
776 between 0 and 7 DPI in either regular diet or HFHS diet hamsters with a false discovery rate of
777 15 % equating to $p = 0.0256$, 0.0193 for RD and HFHS, respectively. *FA22:6 (HFHS $p = 0.0374$)
778 is displayed for comparison to clinical data despite not passing FDR filters. Abbreviations: TNF =
779 tumor necrosis factor, IFN = interferon, IL = interleukin, RD = regular diet, HFHS = high -fat high-
780 sugar, DPI = days post inoculation, sg = subgenomic, VN = virus neutralization. p-values are
781 indicated where appropriate.
782



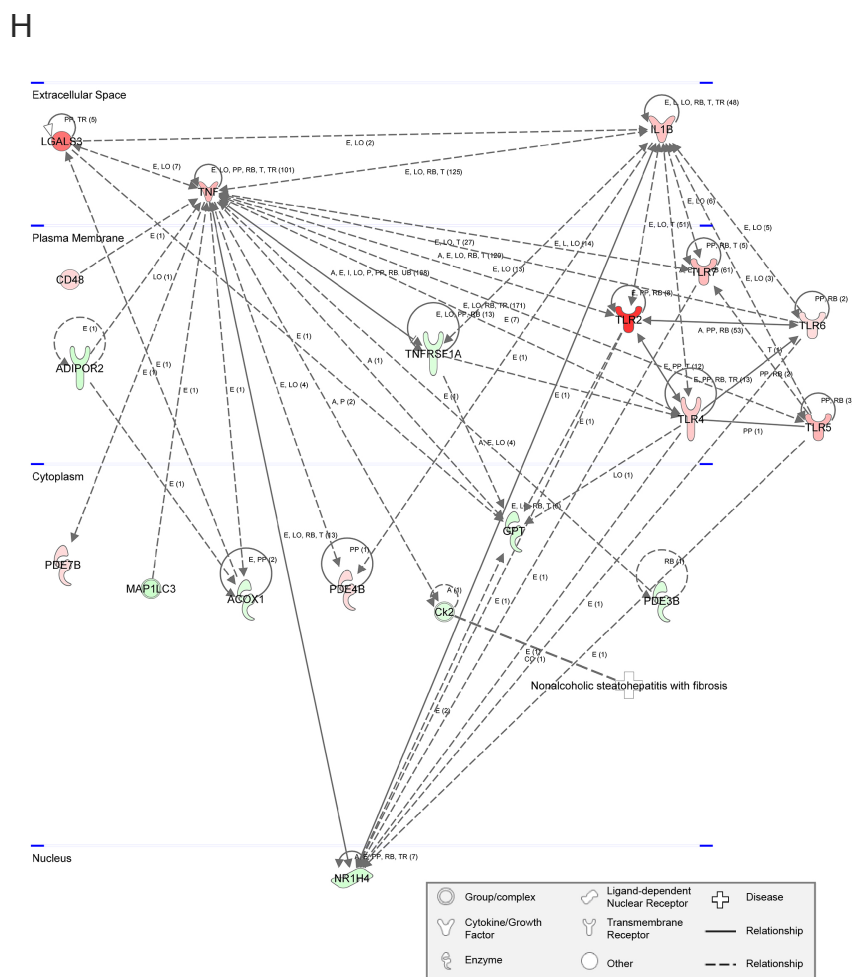
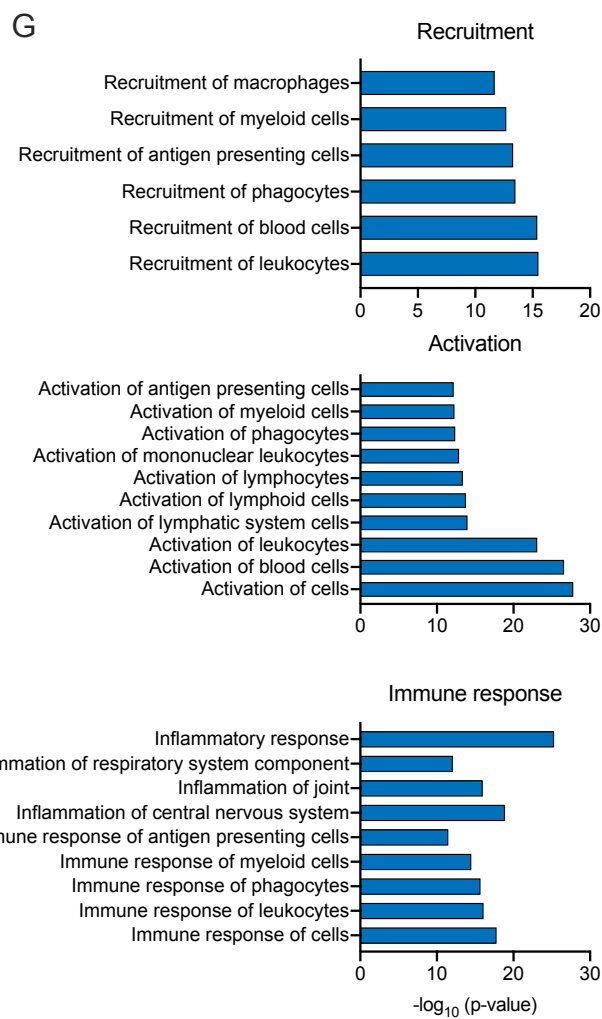
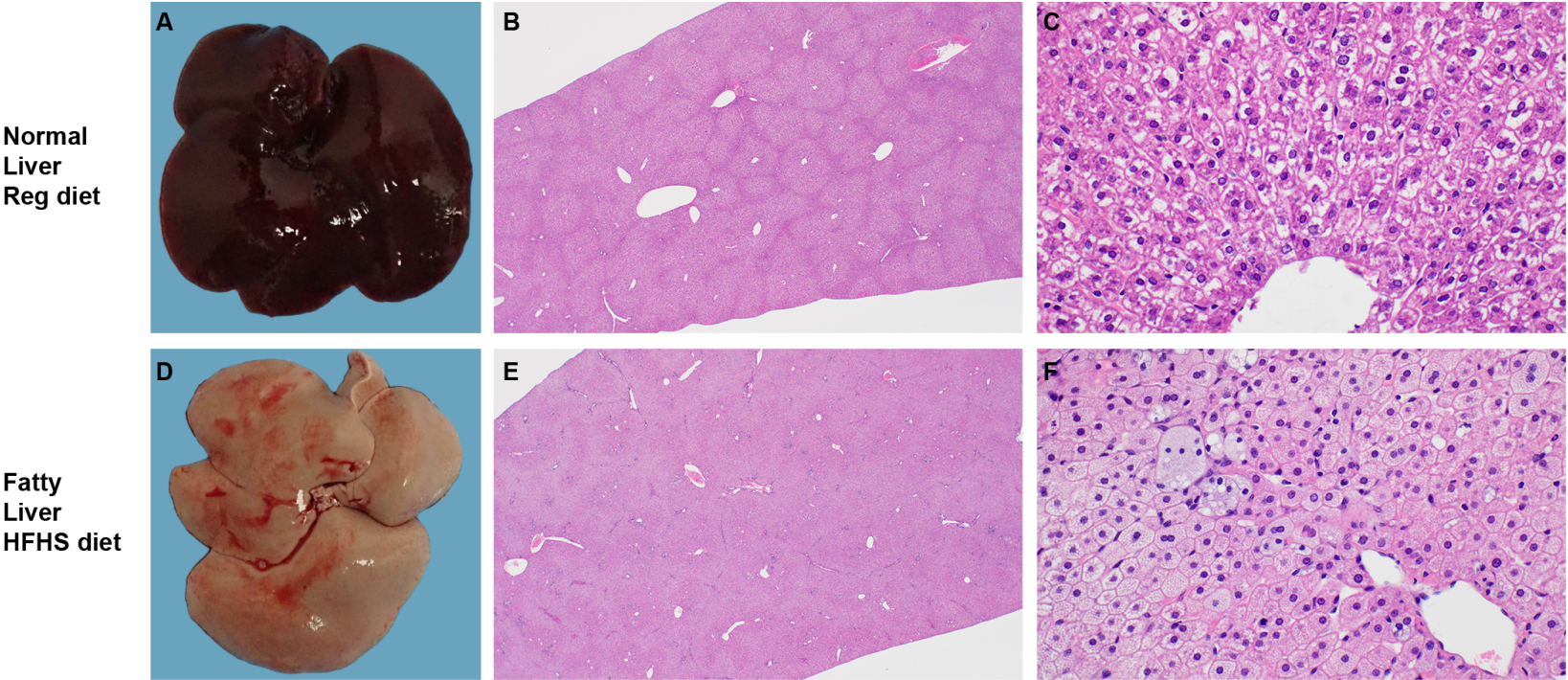


Figure 2

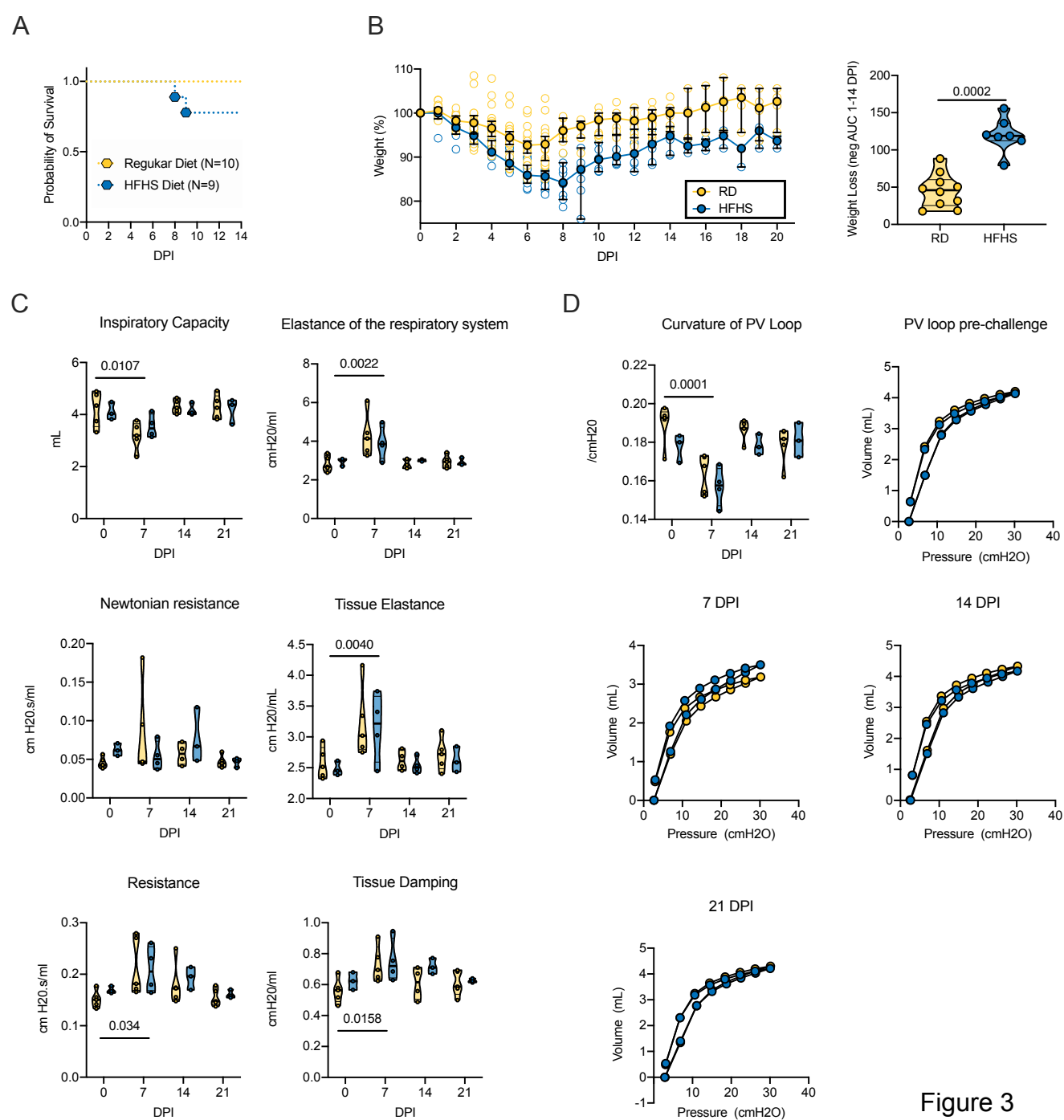
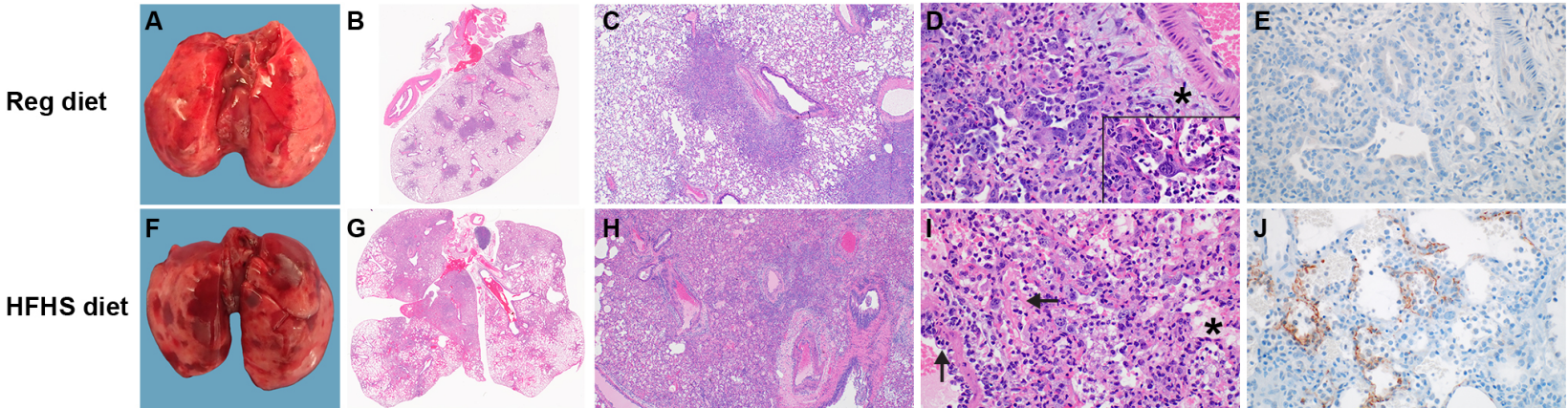


Figure 3



K

	RD 1	RD 2	RD 3	RD 4	RD 5	RD 6	RD 7	RD 8	RD 9	RD 10	HFHS 1	HFHS 2	HFHS 3	HFHS 4
Percentage affected	70	30	20	30	40	70	50	40	60	60	70	60	50	30
Interstitial Pneumonia	4	2	2	3	3	4	3	3	4	4	4	3	3	2
Syncytial Cell	1	1	1	1	1	1	1	1	1	1	1	1	1	1
Alveolar and bronchial exudate	3	2	2	2	2	3	3	3	3	3	4	4	4	3
Bronchiolar epithelial cell inflamm/necrosis	0	0	0	0	0	0	0	0	0	0	1	1	1	1
Perivascular leukocyte cuffing	0	0	0	0	0	0	0	0	0	0	0	0	0	0
vasculitis - neutrophilic	2	2	1	1	2	1	1	1	2	2	3	3	3	2
Type II pneumocyte hyperplasia	1	1	1	1	1	1	1	1	1	1	1	1	1	1
Hemorrhage, fibrin and or edema	3	2	2	1	1	4	3	0	4	4	4	3	3	3

0 = No lesions
 1 = Minimal (1-10%)
 2 = Mild (11-25%)
 3 = Moderate (26-50%)
 4 = Marked (51-75%)
 5 = Severe (76-100%)

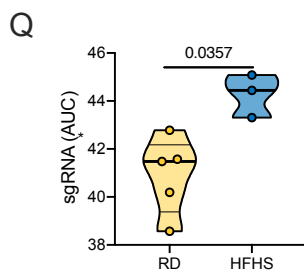
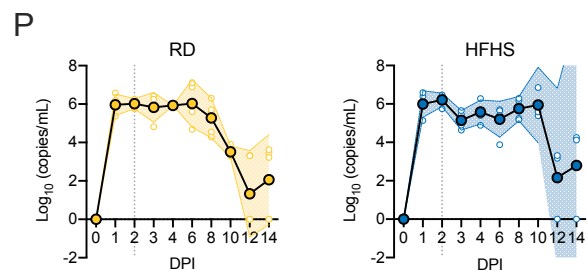
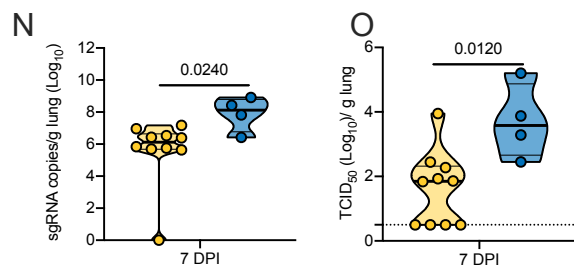
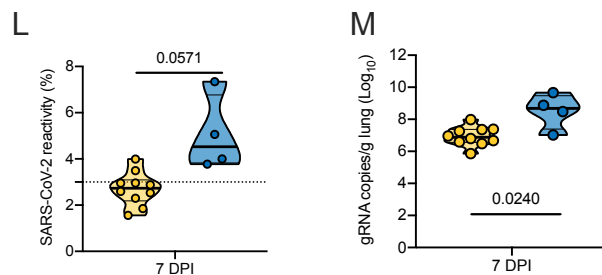
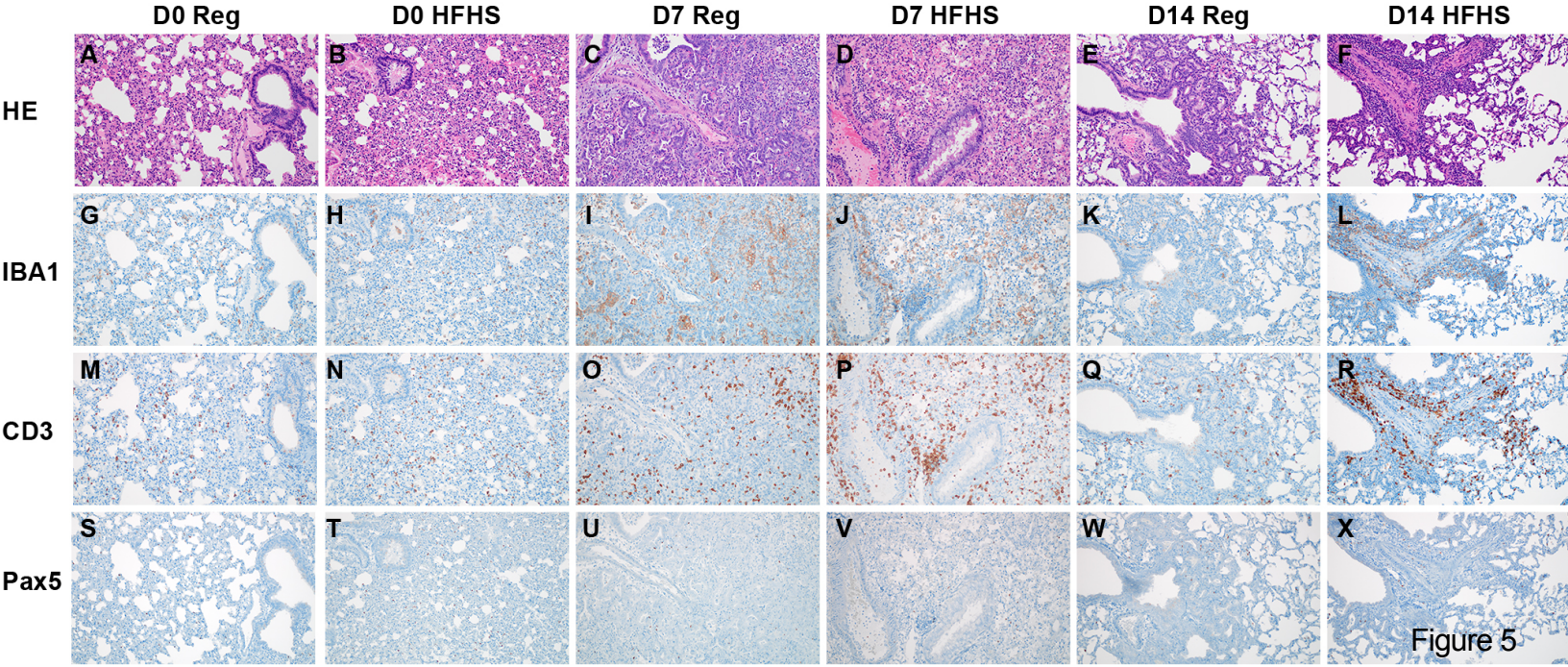


Figure 4



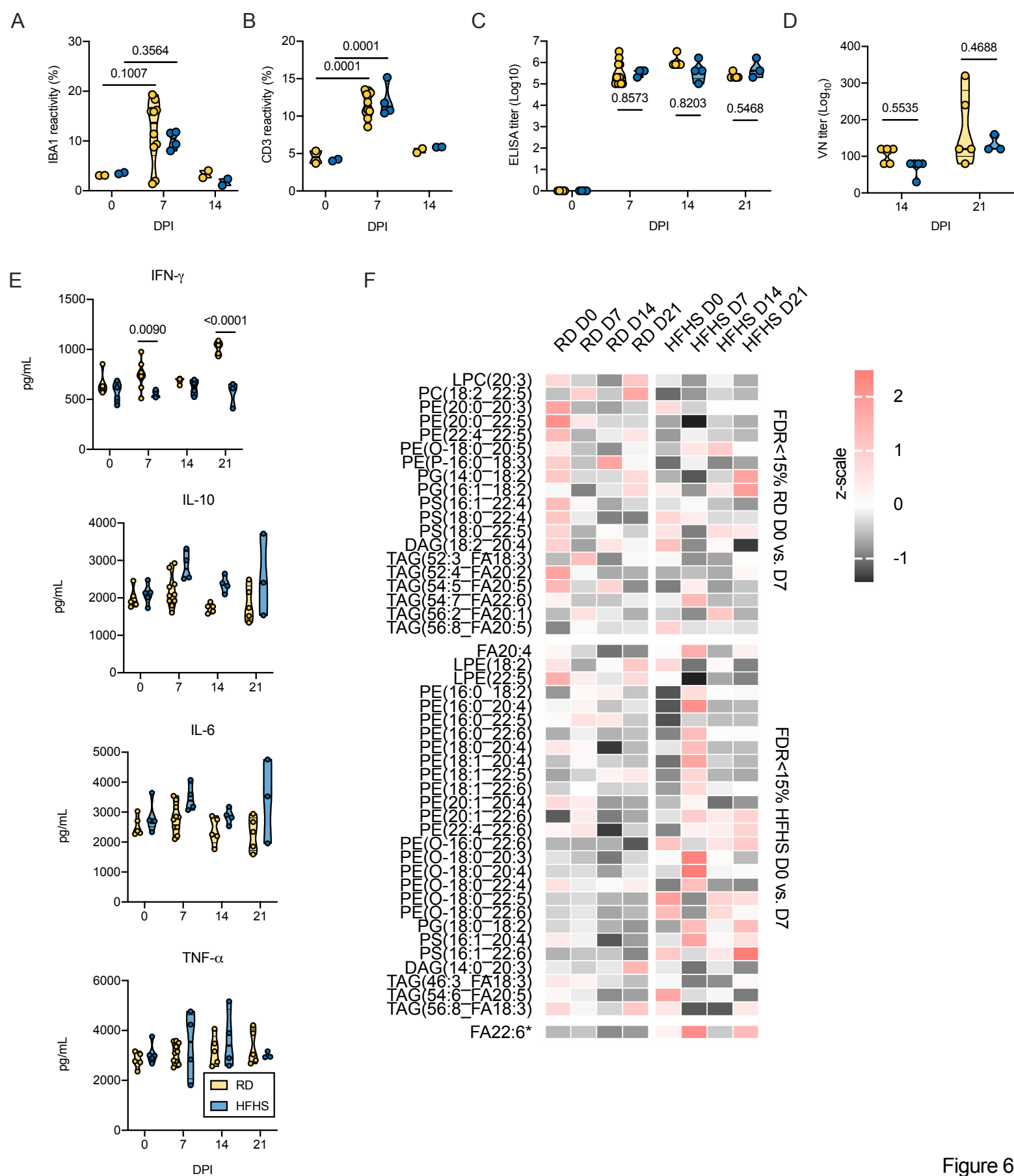


Figure 6

Supplemental Material

Western diet increases COVID-19 disease severity in the Syrian hamster

Julia R. Port^{1*}, Danielle R. Adney^{1*}, Benjamin Schwarz², Jonathan E. Schulz¹, Daniel E.

Sturdevant³, Brian J. Smith⁴, Victoria A. Avanzato¹, Myndi G. Holbrook¹, Jyothi N.

Purushotham¹, Kaitlin A. Stromberg², Ian Leighton², Catharine M. Bosio², Carl Shaia⁴, Vincent J.

Munster^{1#}

1. Laboratory of Virology, National Institute of Allergy and Infectious Diseases, National Institutes of Health, Hamilton, MT, USA
2. Laboratory of Bacteriology, National Institute of Allergy and Infectious Diseases, National Institutes of Health, Hamilton, MT, USA
3. Genomics Unit, Research Technologies Branch, National Institute of Allergy and Infectious Diseases, National Institutes of Health, Hamilton, MT, USA
4. Rocky Mountain Veterinary Branch, Division of Intramural Research, National Institutes of Health, Hamilton, MT, USA

*These authors contributed equally

#Corresponding author: Vincent Munster, email: vincent.munster@nih.gov

Supplemental Table 1: Liver marker profile in serum of regular diet (RD) and high-fat high-sugar diet (HFHS) after 16 weeks. Quantitative determination of total cholesterol (CHOL), high-density lipoprotein cholesterol (HDL), triglycerides (TRIG), alanine aminotransferase (ALT), aspartate aminotransferase (AST), and glucose (GLU) in heparinized whole blood. From the CHOL, HDL and TRIG determinations, low-density lipoprotein cholesterol (LDL), very low-density lipoprotein cholesterol (VLDL), non-HDL cholesterol, and a total cholesterol/high-density lipoprotein cholesterol ratio (TC/H) was calculated. ~ + could not be calculated, LIP = not detectable due to lipid interference.

Animal ID	Chol mg/dl	HDL mg/dl	Trig mg/dl	ALT U/L	AST U/L	GLU mg/d l	nHD Lc mg/d l	TC/ H	LDL mg/d l	VLD L mg/d l	LIP
HFHS.1	360	LIP	~~~	124	78	120	~~~	~~~	LIP	LIP	3
HFHS.2	>520	HEM	HEM	224	HEM	LIP	~~~	~~~	~~~	~~~	3
HFHS.3	~~~	HEM	~~~	140	HEM	LIP	~~~	~~~	~~~	~~~	3
HFHS.4	>520	HEM	HEM	190	HEM	LIP	~~~	~~~	~~~	~~~	3
HFHS.5	380	LIP	>500	117	82	114	~~~	~~~	LIP	LIP	3
HFHS.6	263	LIP	>500	152	86	110	~~~	~~~	LIP	LIP	3
HFHS.7	384	~~~	~~~	188	147	LIP	~~~	~~~	~~~	~~~	3
HFHS.8	331	LIP	>500	114	84	59	~~~	~~~	LIP	LIP	2
Regular.1	83	49	212	62	76	113	34c	1.7c	0	42c	1
Regular.2	52	31	168	100	152	151	21c	1.7c	0	34c	0
Regular.3	98	68	248	67	79	72	30c	1.4c	0	50c	0
Regular.4	111	92	252	87	87	79	19c	1.2c	~~~	50c	1
Regular.5	74	43	184	73	96	98	31c	1.7c	0	37c	1
Regular.6	59	32	201	87	113	119	27c	1.8c	0	40c	1
Regular.7	43	23	204	148	127	101	20c	1.8c	~~~	41c	0
Regular.8	71	42	198	80	88	85	29c	1.7c	0	40c	0
Regular.9	64	46	232	142	157	88	18c	1.4c	~~~	46c	0
Regular.10	49	28	251	123	166	99	21c	1.7c	~~~	50c	0

Supplemental Table 2: Up-and down-regulated pathways in livers pre-challenge organized by disease and function.

Diseases or Functions Annotation	p-value	Predicted Activation State	Activation z-score	# Molecules
Development of genitourinary system	2.07E-11	Increased	2.114	160
Internalization of cells	1.99E-11	Increased	5.333	63
Abnormal bone density	1.99E-11	Decreased	-2.297	50
Phagocytosis of blood cells	1.89E-11	Increased	4.815	52
Adhesion of lymphocytes	1.54E-11	Increased	3.747	34
Interaction of T lymphocytes	1.36E-11	Increased	3.906	39
Adhesion of lymphatic system cells	1.33E-11	Increased	3.839	35
Cell movement of macrophages	1.32E-11	Increased	4.236	65
Adhesion of tumor cell lines	9.66E-12	Increased	2.42	68
Pancreatobiliary tumor	9.07E-12	Increased	2.146	402
Size of body	9.03E-12	Increased	2.966	126
Cell cycle progression	8.08E-12	Increased	2.341	171
Binding of T lymphocytes	7.98E-12	Increased	3.521	37
Interaction of lymphocytes	5.70E-12	Increased	3.973	45
Pancreatic lesion	5.57E-12	Increased	2.114	358
Migration of neutrophils	5.56E-12	Increased	3.941	38
Response of myeloid leukocytes	5.43E-12	Increased	2.565	34
Chemotaxis of neutrophils	5.10E-12	Increased	2.328	42
Migration of granulocytes	4.82E-12	Increased	3.2	43
Cell-cell contact	4.15E-12	Increased	2.864	136
Development of head	3.98E-12	Increased	3.325	164
Quantity of metal ion	3.75E-12	Increased	2.912	85
Aggregation of blood platelets	3.23E-12	Increased	3.084	49
Immune response of antigen presenting cells	3.23E-12	Increased	3.968	49
Binding of lymphatic system cells	2.58E-12	Increased	3.801	45
Transmigration of leukocytes	2.57E-12	Increased	2.603	42
Binding of lymphocytes	2.47E-12	Increased	3.619	43
Transport of molecule	2.41E-12	Increased	2.741	246
Malignant connective or soft tissue neoplasm	2.36E-12	Increased	2.079	203
Response of antigen presenting cells	1.93E-12	Increased	4.049	52
Recruitment of macrophages	1.92E-12	Increased	2.61	33

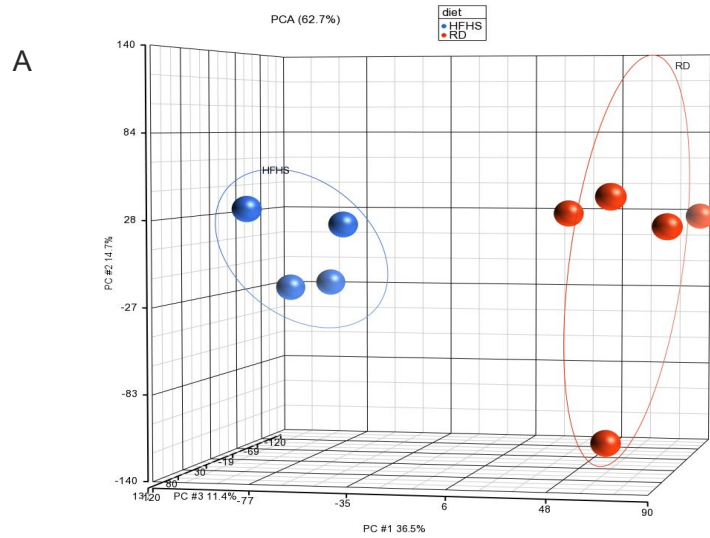
Engulfment of cells	1.87E-12	Increased	4.959	99
Phagocytosis	1.52E-12	Increased	5.163	81
Homing of neutrophils	1.47E-12	Increased	2.328	43
Phagocytosis of cells	1.45E-12	Increased	5.586	75
Binding of endothelial cells	1.13E-12	Increased	2.496	49
Transmigration of cells	1.13E-12	Increased	2.844	49
Cell movement of cancer cells	8.81E-13	Increased	2.68	41
Interaction of endothelial cells	8.80E-13	Increased	2.389	50
Cellular infiltration by myeloid cells	8.74E-13	Increased	2.023	72
Inflammation of respiratory system component	7.19E-13	Increased	2.017	105
Binding of lymphoid cells	7.09E-13	Increased	3.713	44
Activation of antigen presenting cells	6.15E-13	Increased	3.438	70
Homeostasis of blood cells	5.80E-13	Increased	3.757	111
Activation of myeloid cells	4.67E-13	Increased	3.734	74
Degranulation of phagocytes	4.12E-13	Increased	3.533	90
Activation of phagocytes	3.71E-13	Increased	3.826	79
Engulfment of myeloid cells	3.71E-13	Increased	4.655	47
Degranulation of myeloid cells	3.58E-13	Increased	3.647	91
Synthesis of reactive oxygen species	2.88E-13	Increased	4.241	99
Homeostasis of leukocytes	2.75E-13	Increased	3.757	110
Malignant neoplasm of retroperitoneum	2.37E-13	Increased	2.021	419
Quantity of Ca ²⁺	2.14E-13	Increased	2.613	82
Engulfment of leukocytes	2.00E-13	Increased	4.233	51
Recruitment of myeloid cells	1.80E-13	Increased	4.402	64
T cell development	1.58E-13	Increased	3.822	104
Degranulation of leukocytes	1.56E-13	Increased	3.4	95
Upper gastrointestinal tract tumor	1.49E-13	Increased	2.236	581
Invasion of cells	1.48E-13	Increased	4.617	184
Engulfment of phagocytes	1.43E-13	Increased	4.266	49
Cell movement of tumor cell lines	1.37E-13	Increased	4.127	185
Metabolism of reactive oxygen species	1.34E-13	Increased	4.381	104
Growth of connective tissue	1.31E-13	Increased	2.459	123
Amyloidosis	1.30E-13	Decreased	-2.433	116
Activation of mononuclear leukocytes	1.19E-13	Increased	3.257	95

Upper gastrointestinal tract cancer	1.13E-13	Increased	2	580
Lymphopoiesis	9.10E-14	Increased	3.693	123
Adhesion of mononuclear leukocytes	7.27E-14	Increased	3.616	42
Quantity of immunoglobulin	6.65E-14	Increased	3.038	63
Production of antibody	6.01E-14	Increased	3.204	66
Cell viability	5.81E-14	Increased	4.969	235
Phagocytosis of phagocytes	4.62E-14	Increased	4.14	46
Phagocytosis of leukocytes	4.60E-14	Increased	4.229	47
Recruitment of antigen presenting cells	4.55E-14	Increased	3.038	38
Phagocytosis of myeloid cells	3.83E-14	Increased	4.396	46
Activation of lymphocytes	3.64E-14	Increased	3.171	93
Cell movement of T lymphocytes	3.42E-14	Increased	3.59	63
Recruitment of phagocytes	3.01E-14	Increased	4.827	62
Cell survival	1.69E-14	Increased	4.795	247
Activation of lymphoid cells	1.50E-14	Increased	3.25	94
Migration of myeloid cells	1.43E-14	Increased	3.972	54
Production of protein	1.43E-14	Increased	3.73	70
Quantity of B lymphocytes	1.29E-14	Increased	2.549	81
Activation of lymphatic system cells	1.09E-14	Increased	3.088	95
Metastasis	1.03E-14	Increased	3.523	181
Interaction of mononuclear leukocytes	9.60E-15	Increased	3.685	55
Growth of epithelial tissue	7.66E-15	Increased	2.312	135
Quantity of T lymphocytes	7.33E-15	Increased	4.155	111
T cell homeostasis	7.05E-15	Increased	3.667	109
Hematopoiesis of mononuclear leukocytes	6.16E-15	Increased	3.759	132
Migration of antigen presenting cells	4.15E-15	Increased	3.735	51
Immediate hypersensitivity	4.06E-15	Increased	2.362	77
Response of myeloid cells	3.82E-15	Increased	4.283	60
Immune response of myeloid cells	2.85E-15	Increased	4.069	56
Non-colon gastrointestinal cancer	2.59E-15	Increased	2	612
Aggregation of cells	2.51E-15	Increased	3.773	77
Extraadrenal retroperitoneal tumor	2.51E-15	Increased	2.58	463
Chemotaxis of myeloid cells	2.36E-15	Increased	3.493	70
Leukopoiesis	2.22E-15	Increased	4.158	149

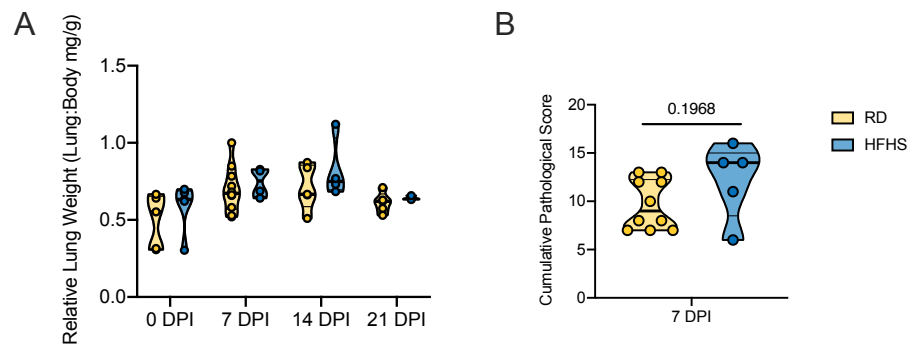
Aggregation of blood cells	1.69E-15	Increased	3.56	62
Differentiation of mononuclear leukocytes	1.67E-15	Increased	3.796	134
Hereditary connective tissue disorder	1.43E-15	Decreased	-3.259	128
Binding of mononuclear leukocytes	1.33E-15	Increased	3.331	54
Advanced malignant tumor	8.44E-16	Increased	3.434	197
Connective tissue tumor	7.45E-16	Increased	2.495	222
Advanced stage tumor	5.25E-16	Increased	3.434	198
Chemotaxis of phagocytes	4.47E-16	Increased	3.987	73
Recruitment of blood cells	4.05E-16	Increased	4.395	79
Connective or soft tissue tumor	3.53E-16	Increased	2.525	249
Degranulation of cells	3.26E-16	Increased	3.573	115
Recruitment of leukocytes	2.92E-16	Increased	4.208	78
Chemotaxis of leukocytes	2.63E-16	Increased	4.146	84
Immune response of phagocytes	2.22E-16	Increased	4.017	62
Growth of tumor	2.05E-16	Increased	4.005	179
Degranulation	1.09E-16	Increased	3.507	117
Inflammation of joint	1.07E-16	Increased	3.397	178
Response of phagocytes	9.69E-17	Increased	4.268	66
Chemotaxis of blood cells	9.45E-17	Increased	4.147	85
Recruitment of cells	8.37E-17	Increased	4.692	85
T cell migration	7.55E-17	Increased	4.271	73
Immune response of leukocytes	7.50E-17	Increased	4.727	80
Hypersensitive reaction	6.65E-17	Increased	3.831	97
Vasculogenesis	5.92E-17	Increased	3.35	158
Angiogenesis	5.56E-17	Increased	4.04	184
Development of vasculature	4.93E-17	Increased	3.955	198
Binding of tumor cell lines	4.04E-17	Increased	2.518	93
Homing of leukocytes	3.51E-17	Increased	4.4	89
Cell movement of antigen presenting cells	2.39E-17	Increased	4.024	91
Binding of myeloid cells	2.30E-17	Increased	3.053	60
Cellular homeostasis	2.19E-17	Increased	4.676	269
Experimental autoimmune encephalomyelitis	1.82E-17	Increased	3.58	86
Homing of blood cells	1.80E-17	Increased	4.405	90
Interaction of tumor cell lines	1.57E-17	Increased	2.283	96
Microtubule dynamics	6.51E-18	Increased	3.927	216
Cell movement of granulocytes	5.63E-18	Increased	3.593	93

Cell movement of lymphatic system cells	2.90E-18	Increased	4.135	101
Organization of cytoplasm	2.90E-18	Increased	4.437	262
Cell movement of neutrophils	2.55E-18	Increased	3.635	83
Encephalitis	2.39E-18	Increased	2.541	95
Immune response of cells	1.57E-18	Increased	4.854	130
Cell movement of lymphocytes	1.14E-18	Increased	4.249	100
Allergy	5.20E-19	Increased	3.26	98
Rheumatic Disease	4.02E-19	Increased	3.322	223
Organismal death	3.96E-19	Decreased	-4.3	362
Morbidity or mortality	2.66E-19	Decreased	-4.307	366
Cell proliferation of T lymphocytes	2.10E-19	Increased	2.415	127
Development of body trunk	1.36E-19	Increased	3.651	215
Binding of professional phagocytic cells	1.35E-19	Increased	2.925	61
Inflammation of central nervous system	1.33E-19	Increased	2.333	102
Invasive tumor	1.09E-19	Increased	3.538	224
Migration of lymphatic system cells	8.48E-20	Increased	4.544	95
Lymphocyte migration	5.97E-20	Increased	4.62	94
Organization of cytoskeleton	5.36E-20	Increased	4.437	249
Chemotaxis	4.82E-20	Increased	4.815	123
Migration of mononuclear leukocytes	3.71E-20	Increased	4.931	99
Proliferation of lymphocytes	3.65E-20	Increased	3.292	150
Proliferation of immune cells	3.58E-20	Increased	3.303	158
Proliferation of lymphatic system cells	3.30E-20	Increased	3.653	159
Homing of cells	2.85E-20	Increased	4.933	128
Interaction of phagocytes	2.61E-20	Increased	3.318	64
Quantity of lymphatic system cells	1.12E-20	Increased	4.27	161
Proliferation of blood cells	8.94E-21	Increased	2.84	172
Migration of phagocytes	7.21E-21	Increased	5.059	82
Proliferation of mononuclear leukocytes	3.68E-21	Increased	3.384	154
Quantity of lymphocytes	1.41E-21	Increased	4.164	155
Cell movement of mononuclear leukocytes	7.82E-22	Increased	4.793	119
Quantity of lymphoid cells	7.71E-22	Increased	4.267	156
Cell movement of myeloid cells	9.41E-23	Increased	5.148	136
Atherosclerosis	5.83E-23	Increased	2.673	111

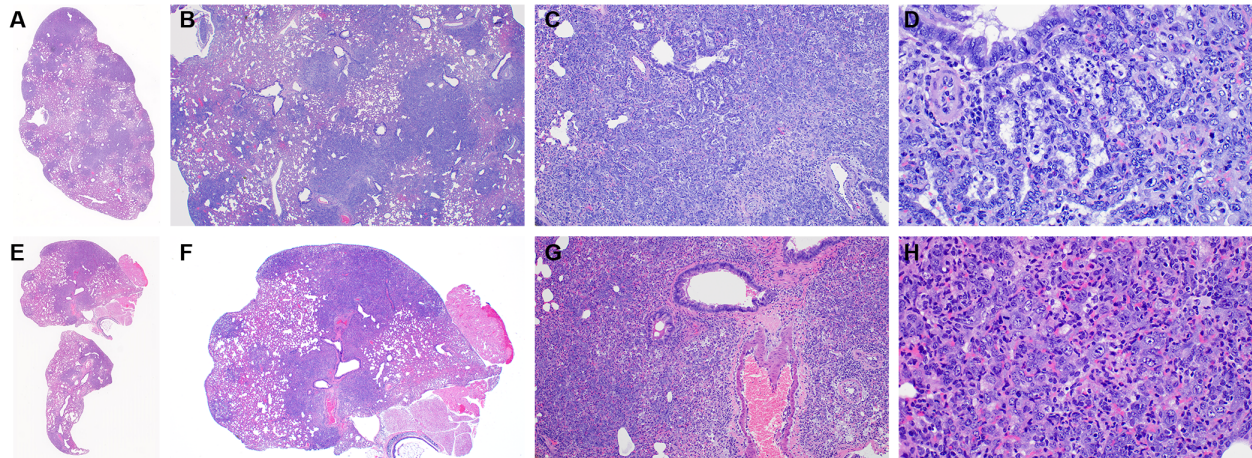
Arteriosclerosis	5.55E-23	Increased	2.673	112
Cancer of cells	5.08E-23	Increased	2.324	684
Occlusion of artery	8.44E-24	Increased	2.291	124
Activation of leukocytes	7.41E-24	Increased	3.906	152
Quantity of mononuclear leukocytes	3.21E-24	Increased	4.23	166
Development of digestive organ tumor	2.85E-24	Increased	2.223	805
Occlusion of blood vessel	1.78E-24	Increased	2.439	127
Cell movement of phagocytes	2.32E-25	Increased	5.16	143
Vaso-occlusion	1.80E-25	Increased	2.762	130
Inflammatory response	5.12E-26	Increased	4.721	179
Neoplasia of cells	4.32E-26	Increased	3.343	764
Nervous system neoplasm	1.09E-26	Increased	2.631	863
Binding of leukocytes	6.17E-27	Increased	4.377	107
Adhesion of immune cells	3.52E-27	Increased	4.659	102
Activation of blood cells	2.67E-27	Increased	4.18	171
Binding of blood cells	1.99E-28	Increased	4.151	117
Activation of cells	1.77E-28	Increased	4.235	212
Adhesion of blood cells	1.50E-29	Increased	4.576	110
Cell movement of leukocytes	2.69E-31	Increased	5.68	193
Leukocyte migration	2.22E-31	Increased	6.163	217
Quantity of cells	2.80E-32	Increased	4.371	346
Migration of cells	2.28E-33	Increased	5.915	387
Quantity of leukocytes	8.59E-34	Increased	3.627	215
Quantity of blood cells	1.14E-34	Increased	3.879	234
Cell movement	1.12E-34	Increased	6.237	422
Digestive organ tumor	2.14E-45	Increased	2.245	1243
Intraabdominal organ tumor	1.16E-50	Increased	2.485	1285
Cancer	3.98E-60	Increased	3.984	1378
Solid tumor	1.91E-61	Increased	2.377	1380
Malignant solid tumor	6.41E-62	Increased	2.227	1377
Non-melanoma solid tumor	2.74E-65	Increased	2.163	1366



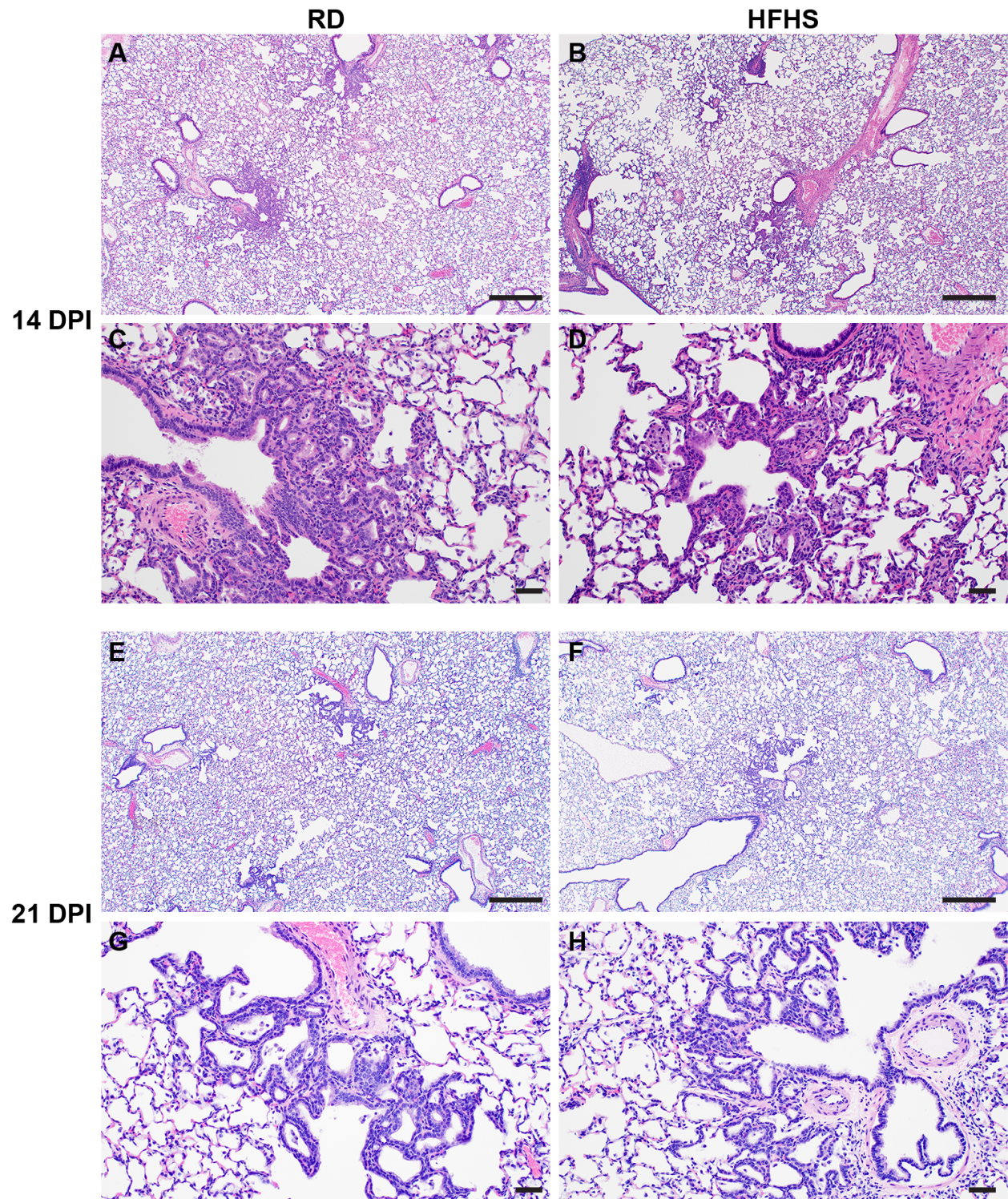
Supplemental Figure 1: A. RNA was isolated for gene expression analyses from liver tissue at 16 weeks and principal component analysis performed. Colors refer to legend on top. Abbreviations: RD = regular diet, HFHS = high-fat high-sugar, PC = principal component.



Supplemental Figure 2: Male Syrian hamsters were fed either a regular or high-fat high-sugar diet *ad libitum* for 16 weeks, then challenged with 8×10^4 TCID₅₀ SARS-CoV-2. Animals were euthanized pre-challenge (0 DPI), at 7, 14 and 21 DPI. **A.** Lung weights. Truncated violin plots depicting median, quartiles, and individuals. **B.** Cumulative pathology score of lung tissues collected at 7 DPI. Truncated violin plots depicting median, quartiles and individuals, N = 10 (RD) / 4 (HFHS), Mann-Whitney test. Abbreviations: RD = regular diet, HFHS = high-fat high-sugar. p-values are indicated where appropriate.

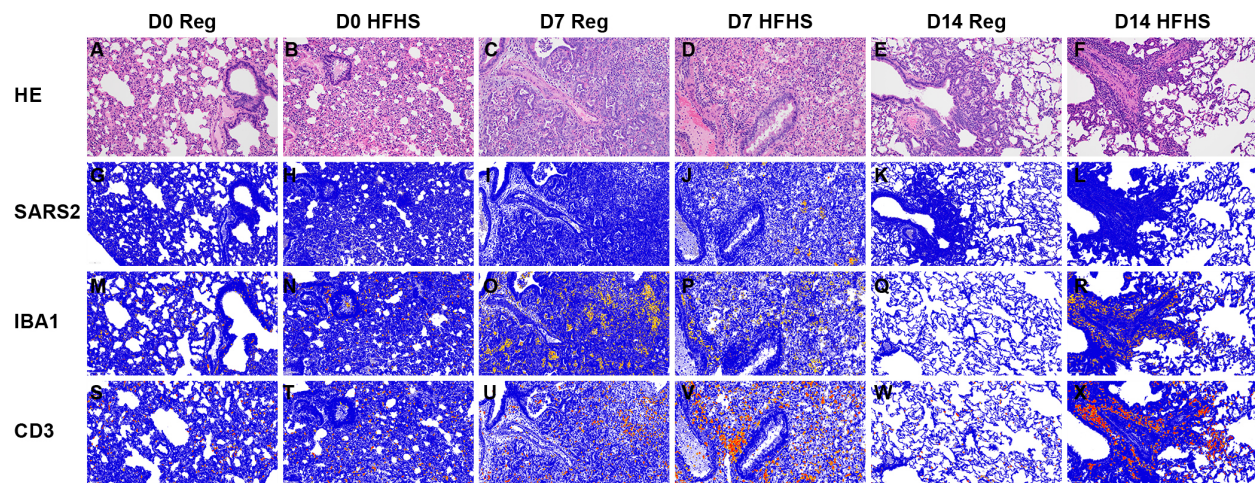


Supplemental Figure 3: Male Syrian hamsters were fed either a regular or high-fat high-sugar diet *ad libitum* for 16 weeks, then challenged with 8×10^4 TCID₅₀ SARS-CoV-2. Animals were euthanized at day 8 and 9 due to increased weight loss. **A, E.** Dark, discreet foci identify areas of pneumonia; lighter areas indicate hemorrhage, edema, inflammation. HE, 1.4x. **B, F.** Although approximately 100% of the lobe is affected, only 50% contains discreet foci of interstitial pneumonia, HE, 20x. **C, D.** Examples of organized type II pneumocyte hyperplasia giving a honeycomb appearance. HE, 100x, 400x. **G, H.** Less well organized foci with more congestion, edema, and inflammation. HE, 100x, 400x. Of note, both appearances overlap and can be present in the same animal.



Supplemental Figure 4: Male Syrian hamsters were fed either a regular or high-fat high-sugar diet *ad libitum* for 16 weeks, then challenged with 8×10^4 TCID₅₀ SARS-CoV-2. Lung tissues were collected 14 and 21 days post inoculation. **A, B.** 14 DPI, Lesions located at terminal bronchioles.

HE, 40x. **C, D.** 14 DPI, Thickened septa, alveolar bronchiolization and minimal inflammation. HE, 400x. **E, F.** 21 DPI, Lesions appear indistinguishable. HE, 40x. **G, H.** 21 DPI, Thickened septa and alveolar bronchiolization remain. HE, 400x. Abbreviations: Reg = regular diet, HFHS = high-fat high-sugar, DPI = days post inoculation.



Supplemental Figure 5: Male Syrian hamsters were fed either a regular or high-fat high-sugar diet *ad libitum* for 16 weeks, then challenged with 8×10^4 TCID₅₀ SARS-CoV-2. Animals were euthanized pre-challenge (0 DPI), 7 and 14 days post inoculation. Serial images of lungs. **A-F.** Pre-challenge lungs appear normal, 7 DPI lungs are pneumonic, and 14 DPI lungs appear to be resolving. HE, 200x. **G-L.** Positive pixel image of IHC staining against N protein of SARS-CoV-2. Note the positive pixels at 7 DPI in the HFHS image, 200x. **M-P.** Positive pixel image of IHC staining against IBA1. Note the increase in positive pixels at 7 and 14 DPI for both the RD and HFHS samples, 200x. **Q-X.** Positive pixel image of IHC staining against CD3, Note the increase in positive pixels at 7 and 14 DPI for both the RD and HFHS samples, 200x. Positive pixel = orange. Abbreviations: Reg = regular diet, HFHS = high-fat high-sugar, DPI = days post inoculation.